2016-12-12

An Investigation of the Cosmic Diffuse X-ray Background

Tomykkutty Velliyedathu
University of Miami, vjbasiltom@yahoo.com

Recommended Citation

Velliyedathu, Tomykkutty, "An Investigation of the Cosmic Diffuse X-ray Background" (2016). *Open Access Dissertations*. 1768.
https://scholarlyrepository.miami.edu/oa_dissertations/1768

UNIVERSITY OF MIAMI

AN INVESTIGATION OF THE COSMIC DIFFUSE X-RAY BACKGROUND

By

Tomykkutty Velliyedathu John

A DISSERTATION

Submitted to the Faculty
of the University of Miami
in partial fulfillment of the requirements for
the degree of Doctor of Philosophy

Coral Gables, Florida

December 2016

UNIVERSITY OF MIAMI

A dissertation submitted in partial fulfillment of
the requirements for the degree of
Doctor of Philosophy

AN INVESTIGATION OF THE COSMIC DIFFUSE X-RAY BACKGROUND

Tomykkutty Velliyedathu John

Approved:

Massimiliano Galeazzi, Ph.D. Professor of Physics	Joshua O. Gundersen, Ph.D. Professor of Physics
Orlando Alvarez, Ph.D. Professor of Physics	Guillermo J. Prado, Ph.D. Dean of Graduate School
Kevin Huffenberger, Ph.D. Professor of Physics Florida State University	

VELLIYEDATHU, TOMYKKUTTY JOHN (Ph.D., Physics)

An Investigation of the Cosmic Diffuse X-ray Background (December 2016)

Abstract of a dissertation at the University of Miami.

Dissertation supervised by Professor Massimiliano Galeazzi.

No. of pages in text. (68)

The cosmic diffuse X-ray background (CXB), which is only second to the cosmic microwave background (CMB) in prominence, has challenged astrophysicists ever since its serendipitous discovery in 1962. In the past five decades, we have made considerable progress unraveling its mysterious origins. Nevertheless, precise identification of its various components and their individual contributions still remains a puzzling task.

The bulk of the XRB comes from the integrated flux of the most luminous astronomical objects—Active Galactic Nuclei (AGN)—as well as the emission from starburst and normal galaxies and can account for most of the emission above ∼1 keV. In the energy range below 1 keV, several components can be identified besides the dominant extragalactic component. While two thermal components, one at ∼1 million K and the other at ∼2.3 million K adequately account for the emission from hot gas in collisional ionization equilibrium, solar wind charge exchange (SWCX) makes a substantial contribution to the SXRB. One of the biggest challenges is to separate the contributions of individual components. This is made difficult by the fact that the spectral structure of all the Galactic components is similar. Shadow experiments have been used to discriminate the various constituents; however, these have only limited use owing to their dependence on estimates of cloud parameters.

The best way to make reliable inferences on the contributions of DXB components is to apply good models to valid data with high statistics. With this in mind, for this work, we selected high quality data, from the well-surveyed sky direction—the

Chandra Deep Field South (CDF-S)—with 4 Ms of observing time, analyzed them and using several models, derived the important parameters for the various DXB constituents obtaining very good constraints. In addition, we used the same data, spread over a period of nine years, to make a systematic analysis of the temporal variation of heliospheric SWCX. Finally, using the results of the DXB analysis we extracted the spectra of the *Chandra* point sources of the CDF-S and obtained important information about the spectral parameters for the different source types.

Table of Contents

List of Figures

List of Tables

Chapter 1

The Diffuse X-ray Background

1.1 Introduction

The diffuse X-Ray Background (XRB) extends over four decades of frequency and is detected over an enormous energy range of $\sim$0.1 keV to $\sim$1 MeV. Owing to the complexity of its spectrum and the diverse nature of the sources contributing to it, the XRB is studied in terms of different energy bands. Typically the cosmic X-ray flux in the interval 0.1–2.0 keV is referred to as the Soft X-Ray Background (SXRB). This study explores the XRB in the 0.5–8 keV energy range (full band) focusing on the 0.5–2 keV bandpass known as the soft band.

After the serendipitous discovery of the XRB along with the detection of the first extra-solar X-ray source Sco X-1 in 1962 (Giacconi et al. 1962) numerous attempts were made to interpret its origination, and its spatial and spectral structure. Analyses of X-ray observations (e.g., Field and Henry 1964; Henry et al. 1968) pointed to an extragalactic origin of the emission. Early indications suggested that the spectrum could be described by a power law of the form

$$S(E) = AE^{-\Gamma} \tag{1.1}$$

where S is the intensity in units of photons s^{-1} keV^{-1} cm^{-2} sr^{-1}, A is a constant, E is the energy and Γ is called the spectral index (Henry et. al 1968). Inverse Compton scattering and synchrotron radiation caused by relativistic electrons could produce such a spectrum. However, there was insufficient evidence to support substantial evolution in the types of sources (e.g., point sources such as quasars) at the time to account for all the observed XRB. This led to the speculation that most of the XRB might be due to truly diffuse emission mechanisms such as thermal Bremsstralung from a hot diffuse gas which could account for the soft diffuse emission at ∼0.25 keV (Henry et. al 1968) as well as above ∼1 keV (Marshall et al. 1980). Analysis of the data from *HEAO-1* A-2 experiment showed that the X-ray spectrum in the range 3–50 keV could be well represented by a thin thermal Bremsstralung model with $kT \approx 40$ keV. However, interpretation of the CMB spectrum from the COBE *FIRAS* instrument (Wright et al. 1994), which did not detect a strong Compton distortion of the CMB spectrum, showed that the density of any diffuse intergalactic medium hot enough to produce the observed diffuse X-ray background is two orders of magnitude too small to produce that background.

Surveys of the X-ray sky using sounding rockets and satellites have given us a good understanding of the sources that produce the SXRB. Sounding Rocket surveys like the Wisconsin Sky Survey and satellite-mounted telescopes like the *Röntgensatellit*, mapped the sky in different X-ray energy bands revealing distinctive spectral and spatial structure that points to the local and extragalactic origin of the SXRB, thus offering important clues about the small scale as well as large scale structure of the Universe.

1.2 The origin and structure of the soft X-ray background

Observations of a number of varied X-ray targets using different observatories have revealed the existence of several components in the SXRB, each having its own distinct origin. They may be broadly classified into two groups: Galactic and extra-Galactic. The Galactic components originate within our own Galaxy from interstellar regions of hot thin gas in collisional ionization equilibrium (CIE) as well as from charge exchange reactions between solar wind ions and interstellar neutrals (SWCX), while the extra-Galactic components which are dominated by the emission due to unresolved point sources come from sources outside the Galaxy. They are generally characterized by their own unique origination and spectral structure.

1.3 Galactic sources of the SXRB

Even though experiments pointed to an extragalactic origin and isotropic nature of the diffuse X-ray background (DXB) above ∼1 keV there remained considerable uncertainty regarding its origins. Existence of an anisotropic Galactic component was also subsequently recognized (Bowyer 1968). Observations in the 1.5–8 keV range showed that the isotropic background breaks at lower energies implying an independent origin (Henry et al. 1968) which was incorrectly attributed to free-free emission from intergalactic gas. All-sky surveys of the diffuse X-ray sources subsequently revealed that the diffuse X-ray background (DXB) below ∼1.2 keV is made up of several distinct components which originate from sources within as well as outside the Galaxy.

1.3.1 Local Hot Bubble

After the discovery of the diffuse X-ray background (DXB) in 1962, a series of dedicated X-ray missions were carried out to study its structure and origin. The Wisconsin Sounding Rocket Sky Survey (McCammon et al. 1983), which started in 1972 obtained maps of the X-ray sky in several energy bands. The X-ray maps of the low energy bands B (130–188 eV) and C (160–284 eV) show a negative correlation of intensity with the H i column density (N_{HI}) (fig 1.1). These maps showed that the SXRB was anisotropic with strong emission towards the halo of the Galaxy but only about 30% as much in the Galactic plane. Using an absorption model, the C band data may be fit to a function of the form

$$F = F_{unabs} + F_{abs}\exp(-N_H\sigma) \tag{1.2}$$

where F_{unabs} is the unabsorbed flux of ∼100 counts per second, F_{abs} is the absorbed flux. Since the effective absorption cross section strongly depends on energy ($\sigma \propto E^{-3}$) and the B band and C band fluxes correlate (their ratio is nearly constant (∼2.5), it is clear from equation (1.2) that the anti-correlation in the two bands is not entirely energy-dependent. Also, there is significant emission in the Galactic plane even though the mean free path is very short and the observed intensity variations with changing column density are much smaller than predicted by atomic absorption cross sections calculated by Brown and Gould (1970). Thus, we are led to conclude that in addition to the absorbed Galactic and extra-Galactic flux, there must be local sources of diffuse X-rays which contribute a substantial fraction of the flux at least in the low energy bands.

Robertson et al. (2003) found that maps of the 1/4 keV X-ray sky are still bright, even after the SWCX flux is subtracted. Due to the small optical depth of the Galactic disk, only soft X-rays that are produced locally and a small fraction of the X-rays that come from very bright non-local sources will contribute to the X-ray intensity in this bandpass. Thus, low-latitude X-rays are almost entirely due to a local origination and the mapped intensity after SWCX subtraction can be attributed to emission from a bubble of hot diffuse gas called the Local Bubble (LB).

The anti-correlation noted above can also be explained if we assume that the solar system is located in a *plasma bubble*. Initial evidence of such a neutral Hydrogen deficient cavity came from UV results. The cavity has an elongated shape lying in an oblique Galactic north-south direction and contains million degree plasma. In directions in which the bubble is longer the emission is stronger thus explaining the anti-correlation. This model, first proposed by Sanders et al. (1977) is called the ”displacement model”, meaning that the bubble is almost depleted of neutral material and filled with high temperature plasma. It was theoretically investigated by Cox & Anderson (1982). A supernova explosion can set off a blast wave propagating through the interstellar medium (ISM) heating it to high temperature plasma. The inferred dimensions of this cavity, called the Local Hot Bubble (LHB) range from ∼70 pc in the Galactic plane to ∼130 pc towards higher latitudes. Optical ISM absorption studies and 21-cm N_{HI} measurements place limits on the average neutral hydrogen column density: $< 7 \times 10^{18}$ cm^{-2} (Juda et al. 1991)

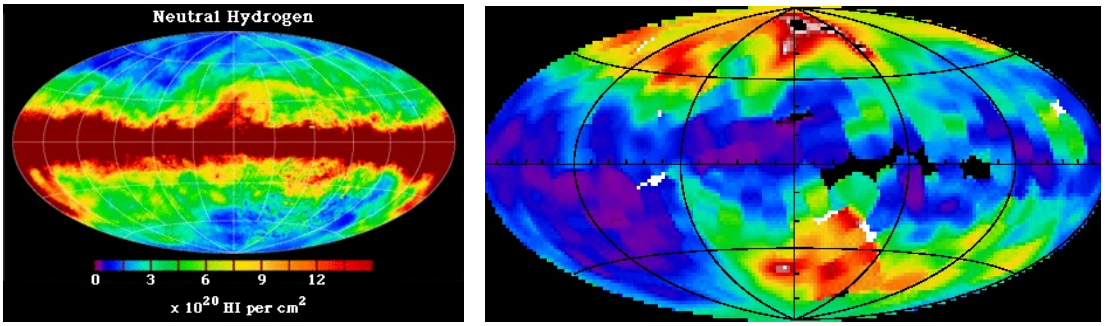

(a) (b)

Figure 1.1: (a) Map (Aitoff-Hammer equal area projection in Galactic coordinates) of the column density of Galactic neutral hydrogen. (b) X-ray map of the Wisconsin C band showing the anti-correlation of hydrogen column density with X-ray background.

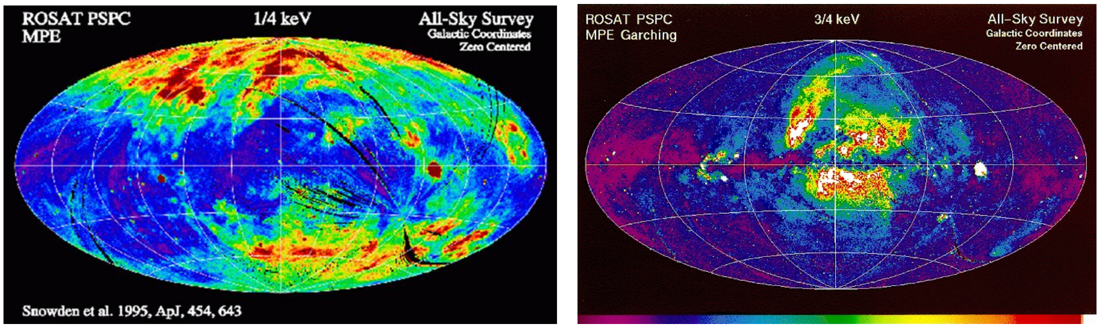

(a) (b)

Figure 1.2: (a) ROSAT 1/4 keV X-ray map (Aitoff-Hammer equal area projection in Galactic coordinates). (b) ROSAT 3/4 keV map.

1.3.2 The Galactic halo

ROSAT, launched in 1990, made all-sky surveys of the X-ray sky in three energy bands, the 1/4 keV, the 3/4 keV and the 1.5 keV, covering ∼98% of the sky with ∼2° angular resolution. These maps show rich, well-defined spatial structure, and the 1/4 keV band—the ROSAT equivalent of the Wisconsin C band—clearly demonstrates and confirms the ”almost ubiquitous negative correlation” (Snowden et al. 1995) already revealed in the Wisconsin B and C maps, when compared with maps of the neutral hydrogen column density.

With the improved angular resolution of the Position-Sensitive Proportional Counter (PSPC), ROSAT was able to identify individual clouds, and shadowing experiments in which X-rays coming along the direction of the cloud (foreground emission) could be discriminated from those coming in off the cloud direction (background emission) were made possible. The Draco cloud, which lies about 200 pc above the Galactic plane, showed clear evidence of shadowing, indicating non-local sources, such as the Galactic halo and extragalactic emission. The discovery of shadowing clouds in the 1/4 keV background with ROSAT showed that $\sim$50% of the 1/4 keV emission originates from beyond the LB (Burrows & Mendenhall 1991; Snowden et al. 1991). This more distant emission originates from the Galactic halo, which contains hot gas with temperatures in the range 10^6–$10^{6.5}$ K (Snowden et al. 1998; Kuntz & Snowden 2000; Smith et al. 2007; Galeazzi et al. 2007). Thus, a single component model cannot adequately quantify the SXRB. The Diffuse X-ray Spectrometer, on board the Space Shuttle and the micro-calorimeter experiments have proved that the SXRB is dominated by a line-filled spectrum. A two-temperature thermal plasma model can be used to fit the spectrum. However, there is excess flux in the higher bands (≈ 1 keV) coming from the attenuated extragalactic flux due to point sources which requires a third component modeled as an extrapolation of the power law. Taking all these into account, Snowden et al. (1998) proposed a multi-component model: a thermal plasma to model the LHB, a hotter absorbed thermal component to account for the halo emission, and an absorbed power law to include the contribution from point sources.

1.3.3 Solar Wind Charge Exchange

Comparing measurements from several observations of the same location in the sky, ROSAT detected a time-varying background component called the Long-term Enhancements (LTE) (Snowden et al. 1994, 1995). It was shown by Cravens et al. (2001) that the LTE were correlated with the solar wind flux, and thus were due to the phenomenon called Solar Wind Charge Exchange (SWCX). SWCX occurs when highly charged ions in the solar wind interact (charge-exchange) with neutral atoms in the interstellar medium (ISM). The resultant ion is in an excited state and in the transition to the ground state a photon is produced in either the soft X-ray or extreme ultraviolet. Since the solar wind is temporally variable in density, speed, elemental abundance, and ionization fraction, the observed SWCX emission varies as a function of time and observation geometry.

The charge-exchange spectrum has the same transitions, with nearly the same strengths, as a purely recombining plasma, and thus makes a strong contribution to the lines used for astrophysical plasma diagnostics. Since the SWCX emission has no unique spectral signature and will be smooth over the FOV of any X-ray instrument, it is not easily distinguishable from other diffuse components such as those expected from the Local Hot Bubble, the Galactic bulge and halo, and the Warm-Hot Intergalactic Medium. Prominent SWCX emission lines include those from C VI, O VII, O VIII, Ne IX, and Mg XI that are also important diagnostics of astrophysical plasmas. Thus, removal of SWCX as a contaminant becomes difficult because modeling of the SWCX emission would be problematic owing to the lack of sufficiently detailed abundance and ionization state information for the solar wind (Kuntz et al. 2015).

SWCX emission comes mainly in two forms: heliospheric and geocoronal. Heliospheric SWCX emission originates from the collision of the solar wind ions with neutrals in the ISM which contains H and He and its strength depends on time and observation geometry. It is observed throughout the heliosphere. It is also affected by solar activity. Geocoronal (magnetosheath) SWCX is due to the interaction of solar wind with neutral H in the earth's exosphere and is brightest in the region between the Earth and the Sun (the sub-solar region; Robertson & Cravens 2003). Because of the density fluctuations in the magnetosphere caused by changes in the solar wind flux, geocoronal SWCX also shows temporal as well as look-direction dependence.

1.4 Extra-Galactic X-ray background

Observations using telescopes with very high spatial resolution confirmed that most of the extragalactic diffuse emission came from unresolved faint sources. *Chandra* with its supreme spatial resolution of $\sim 1''$ has resolved $\sim$90 percent of the diffuse extragalactic emission into a finite number of point sources. That leaves ∼10 per cent of the DXB as truly diffuse background and needs to be accounted for. Careful analysis of the background maps and the spectrum suggests that this cosmic component could originate from non-virialized structures of inter-galactic and inter-cluster hot gas often called the Warm Hot Inter-galactic Medium (WHIM).

1.4.1 Point sources

Point sources comprising Active Galactic Nuclei (AGN), normal and star-burst galaxies contribute most of the CXB above 1 keV. Below 1 keV point sources make up about 50 percent of the X-ray flux even though the intensity depends on the Galactic latitude and the energy bandpass. The spectrum of a point source is primarily due to synchrotron radiation by relativistic electrons in the magnetic field surrounding the point source and is characterized by a *power law* shape. This gives rise to a radiated photon spectrum that is also a power law. Inverse Compton scattering also produces a power law spectrum that is indistinguishable from from that due to synchrotron radiation. Thermal electrons can upscatter low energy photons to the X-ray energy range and even to gamma wavelengths. A logarithmic plot of intensity versus frequency gives a straight line with a negative slope which is used to characterize the point source spectrum.

At the current sensitivity limit of *Chandra*, AGN provide more than 75% of the extragalactic emission. However, predictions based on cumulative number counts show that normal galaxies too faint to be resolved by current detectors could outnumber the AGN population when new discovery space is fully explored. The recent *Chandra* 7 Ms ultra deep survey of the *Chandra* Deep Field South (CDFS) should be able to shed more light on these ultra deep sources and their contribution to diffuse X-ray emission.

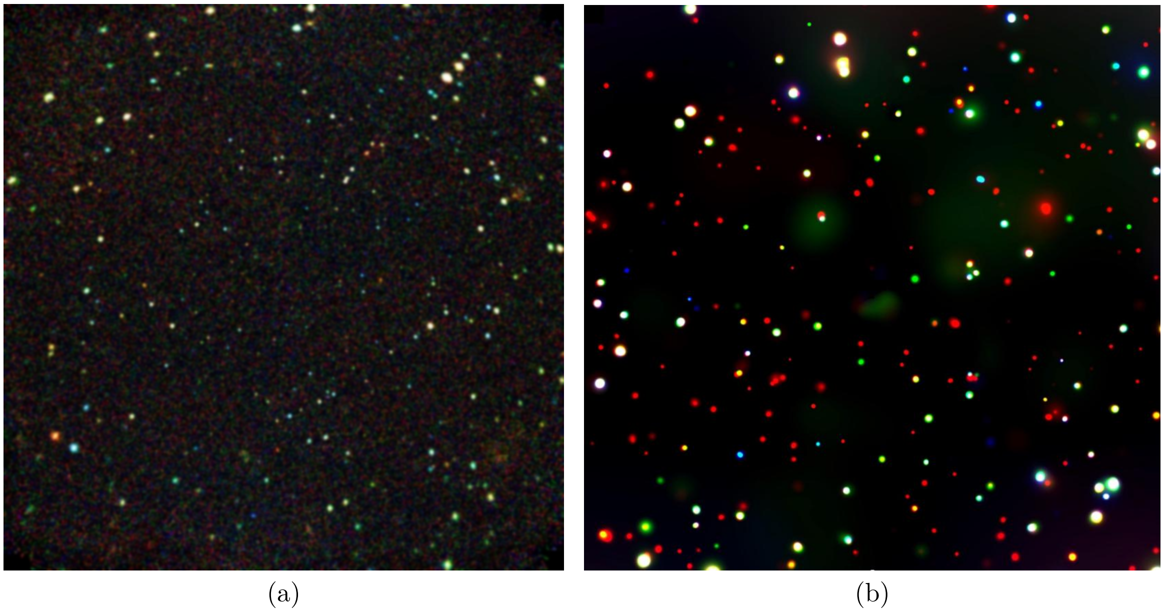
(a) (b)

Figure 1.3: (a) The *Chandra* Deep Field South (CDFS) 4 Ms survey. (b) The CDFS 7 Ms survey.

1.4.2 Warm Hot Inter-galactic Medium (WHIM)

Cosmologists have noticed a discrepancy between the baryon density actually observed in the local universe (Fukugita, Hogan, & Peebles 1997) and the predicted baryon density based on analysis of absorption lines in the Lyman alpha forest (Rauch et al. 1998; Weinberg et al. 1997) as well as that based on observed light-element ratios combined with standard nucleosynthesis. The amount of baryons missing in the present-day universe is $\sim$75%. A possible explanation for the missing baryons as suggested by large-scale cosmological dynamical simulations (Cen & Ostricker, 1999) is that a substantial fraction of these baryons could be lying undetected in the intergalactic space in a warm-hot (10^5–10^7 K) and tenuous gas phase called *WHIM*, where their weak emission lines are difficult to detect. However, its existence can be deduced from angular autocorrelation analysis of the density fluctuations that trace the filaments connecting the virialized structures which form galaxies and clusters.

Cosmological hydrodynamic simulations (e.g., Cen and Ostricker 1999; Brian et al. 1998) have been used to estimate the distribution and evolution of baryons over several epochs in terms of their typical temperature and density phase. They are presumed to exist in the temperature range 10^5–10^7 K where their detection poses difficulties. Their signatures are practically indistinguishable from those of other soft diffuse components such as the absorption lines O VI (1032, 1038)A and O VII (0.574 keV), emission lines O VIII (0.653 keV) and low redshift Lymann alpha lines.

When the primordial density perturbations become non-linear after decoupling at z $\approx$ 1000, the shock waves generated by the gravitational collapse resulting in the formation of large scale structures (e.g., clusters) heat up the circumstructural gas into a warm/hot phase typically in the range 10^5–10^7 K. Simulations suggest that the hot component of the WHIM increases in mass fraction from high redshift towards z $\sim$0. The mechanism by which such an inter galactic medium (IGM) is sustained at the presumed temperature is quite complex, and is dictated by dynamic interactions between the dark matter, which is believed to permeate the virialized structures, the surrounding gas and the continuously created galaxies. The existence of the hotter phase of WHIM ($\sim 10^7$ K) needs to be reconciled with the COBE *FIRAS* non-detection of any strong Compton distortion of the CMB spectrum pointing to the absence of a significant number of high energy electrons in the IGM. One might as well look for spectral signatures in the absorption lines produced by high redshift quasars and Lymann-break galaxies that are presumed to be the predominant ionizers of the IGM.

Chapter 2

X-ray observatories

2.1 Introductory Remarks

This chapter discusses the prominent features of two space-based telescopes—XMM-*Newton* and *Chandra*—the two pillars of modern X-ray astronomy. This is very relevant in view of the fact that this study makes extensive use of the X-ray data obtained from both these telescopes. XMM-*Newton*, the largest scientific European spacecraft to date, was launched on December 10, 1999 by the European Space Agency (ESA). It follows a highly eccentric 48-hour elliptical orbit, traveling out to nearly one third of the distance to the Moon. The *Chandra* X-ray observatory, previously known as Advanced X-ray Astrophysics Facility, is NASA's flagship X-ray telescope and was launched on June 23, 1999 and subsequently placed in a high elliptical orbit of 64 hours allowing long, uninterrupted observations.

2.2 The X-ray telescope

Since X-rays are very energetic, they easily penetrate the mirrors used in an optical telescope and hence X-ray telescopes need specially designed mirrors that are aligned for grazing incidence such that the X-rays that ricochet off the mirrors are focused on to electronic detectors placed in the focal plane of the telescope. Figure 2.1 shows a Wolter 1 type mirror which is used in both XMM-*Newton* and *Chandra* telescopes.

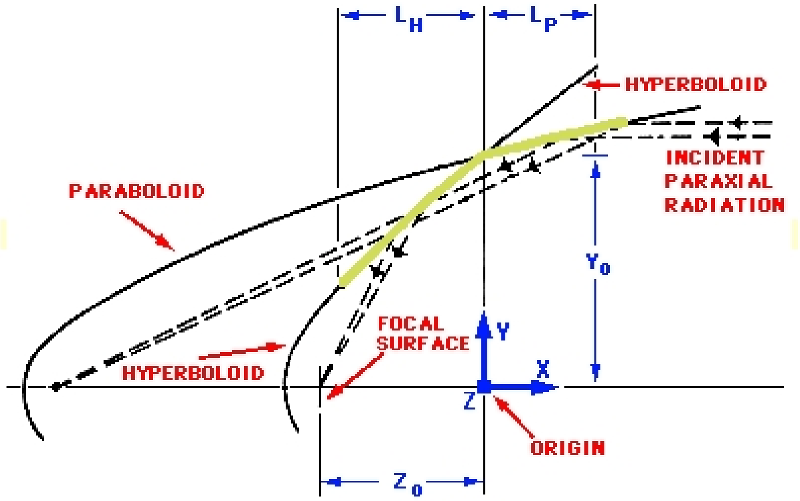

Figure 2.1: Principle of the X-ray telescope, Wolter 1 type.

2.3 XMM-*Newton*

X-ray Multi-Mirror Mission (XMM-*Newton*[1]) observatory exploits replication technology for its reflecting telescopes offering an excellent trade-off between effective area and resolution. There are six co-aligned instruments that operate simultaneously: three telescopes equipped with three EPIC (European Photon Imaging X-ray Camera) imaging X-ray cameras, two RGS (Reflection Grating Spectrometer) X-ray spectrometers and the OM (Optical Monitor). Figure 2.2 shows the several modules of the spacecraft. The Focal Plane Assembly (FPA) is a platform that carries the focal plane instruments: an EPIC PN and two EPIC MOS semiconductor imaging detectors (Charged Coupled Devices or CCDs) and two RGS grating spectrometers. The Mirror Support Platform (MSP) holds the three mirror assemblies, the OM and the two star-trackers. A long carbon fiber telescope tube (not shown in the figure) maintains the FPA and the MSP separation. The Service Module (SVM) contains the spacecraft subsystems, solar array wings and the Telescope Sun Shield.

---

[1] cf. http://xmm.esac.esa.int/external/xmm_user_support/documentation

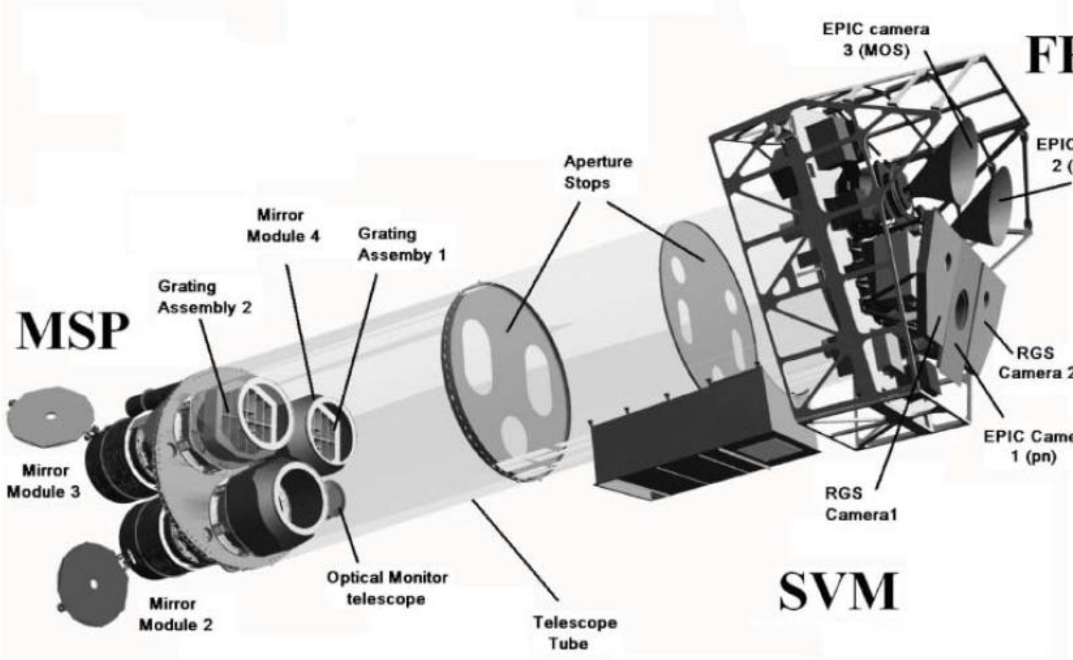

Figure 2.2: XMM-*Newton* spacecraft subsystems

2.3.1 Telescope

Each of the three X-ray telescopes on board XMM-*Newton* consists of 58 Wolter I grazing-incidence mirrors which are nested in a coaxial and cofocal configuration. The optics design was driven by the requirement of obtaining the highest possible effective area over a wide range of energies, with particular emphasis in the region around 7 keV. Thus, the mirror system had to utilize a very shallow grazing angle of $30^{\prime}$ in order to provide sufficient reflectivity at high energies. The 58 Wolter I mirrors of each telescope are bonded on their entrance aperture to the 16 spokes of a single spider. The on-axis PSF (Point Spread Function) of the telescope provides an angular resolution of $\sim 15^{\prime\prime}$ (HEW). The off-axis PSF varies with the off-axis angle as shown in figure 2.3. The major objective of the design for the XMM-*Newton* telescopes was to achieve maximal area at low energies (2 keV) without sacrificing area at high energies (7 keV). XMM mirrors are most efficient in the energy range from 0.1 to 10 keV, with a maximum around 1.5 keV and a pronounced edge near 2 keV (the Au M edge). The goal was to achieve a collecting area of 1900 cm^2 for energies up to 150 eV, 1500 cm^2 at 2 keV, 900 cm^2 at 7 keV, and 350 cm^2 at 10 keV, for each of the telescopes.

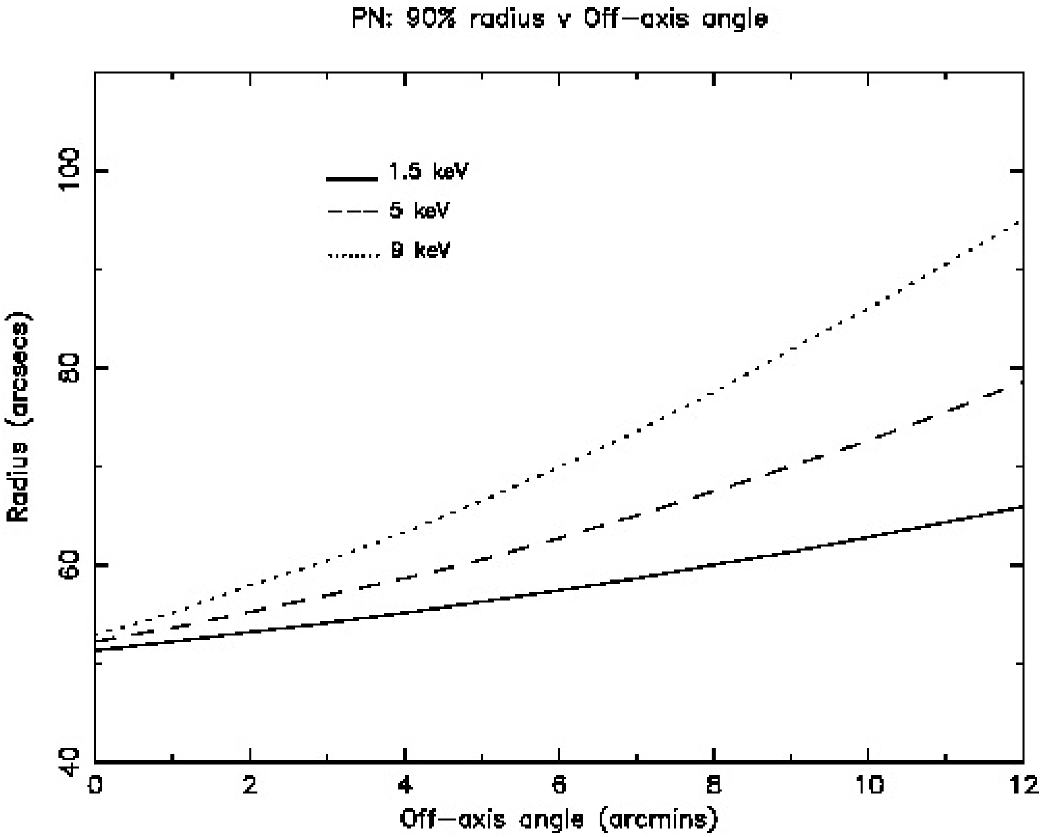

Figure 2.3: The W90 radius of a point source observed with the pn camera as a function of off-axis angle at different energies.

2.3.2 Instruments

2.3.2.1 EPIC

The X-ray cameras contain two types of CCD arrays: EPIC (European Photon Imaging Camera) pn and EPIC MOS. There are two EPIC MOS cameras: MOS1 and MOS2. The three EPIC cameras perform highly sensitive imaging observations over the telescope field of view (FOV) of $30'$ with moderate spectral resolution ($E/\Delta E \sim$ 20–50) in the energy range 0.15 to 15 keV. All EPIC CCDs operate in photon counting mode with a fixed, mode dependent frame read-out frequency.

Mirror		Wolter 1 type
Number of mirrors per telescope		58
Mirror substrate material		nickel
Reflective Coating		gold
Telescope focal length		7.5m
HEW (arcsec)	pn	15.1
	MOS1	13.6
	MOS2	12.8
FWHM (arcsec)	pn	6.6
	MOS1	6
	MOS2	4.5
FOV (arcmin)		30
Effective area (cm^2) @1kev		1500

Table 2.1: XMM telescope parameters

2.3.2.2 Reflection Grating Spectrometer (RGS)

The RGS contains an array of reflection gratings placed in the paths of the converging beams of two of the three mirror modules. The gratings divert about half of the incident flux towards the RGS detectors such that ∼44% of the original incoming flux gets to the MOS cameras. The RGS instruments achieve high resolving power (150 to 800) over a range from 5 to 35 Å (0.33 to 2.5 keV).

2.3.2.3 Optical Monitor (OM)

The Optical/UV Monitor provides coverage in the band 170–650 nm allowing multi-wavelength observations simultaneously in the X-ray and UV/Optical bands. The telescope is of a Ritchey-Chrétien design and has an aperture of 30 cm. With its very sensitive detectors, filters and grisms, the OM is a powerful instrument for observing faint stars.

2.4 ***Chandra***

The *Chandra* X-ray observatory, launched by Space Shuttle Columbia on June 23, 1999, is the third of NASA's great observatories, and is equipped with instruments that offer the best angular and spectral resolution. The precisely shaped and aligned

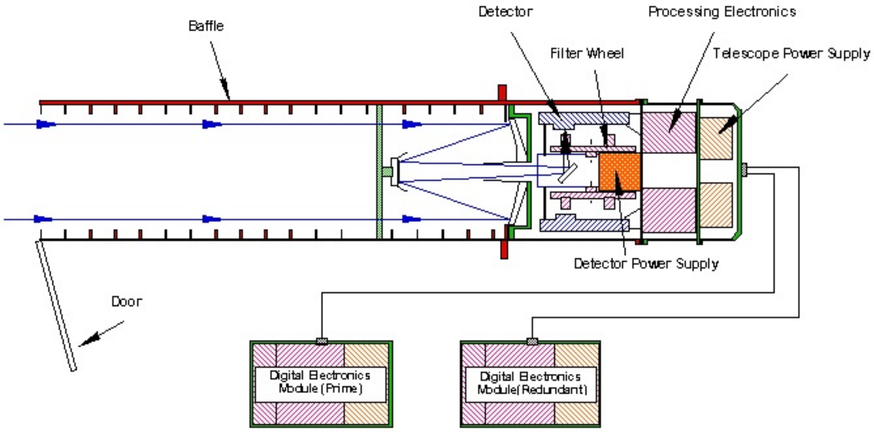

Figure 2.4: Schematic of Optical Monitor

mirrors in conjunction with the four science instruments capture and probe X-rays from a variety of astronomical sources located over a range of redshifts. The focal plane science instruments, HRC (High Resolution Camera), and ACIS (Advanced Charge Coupled Imaging Spectrometer) are perfectly matched to capture the highest-resolution images formed by the mirrors and to provide information about the incoming X-rays: their number, position, energy and time of arrival.

2.4.1 *Chandra* Instruments

2.4.1.1 HRC

The HRC accurately records the position, number, and energy of X-rays. The camera consists of two clusters of 69 x 06 lead oxide (PbO2) glass tubes, 1.2 mm long and 0.10 mm in diameter ($\sim$1/8th the diameter of a human hair.) The X-rays strike the tubes and release electrons that are accelerated down the tubes at high voltage. The electrons trigger the release of other electrons, and at the end of the tubes millions of electrons strike a grid and produce a finely detailed map of the source which emitted the X-rays. It uses large field-of-view micro-channel plates (MCP), one optimized for imaging (HRC-I) and the other for spectroscopy (HRC-S), to make X-ray images, with a high angular resolution of $\sim 0.5''$ over a $(31' \times 31')$ FOV and time resolution of 16 μs.

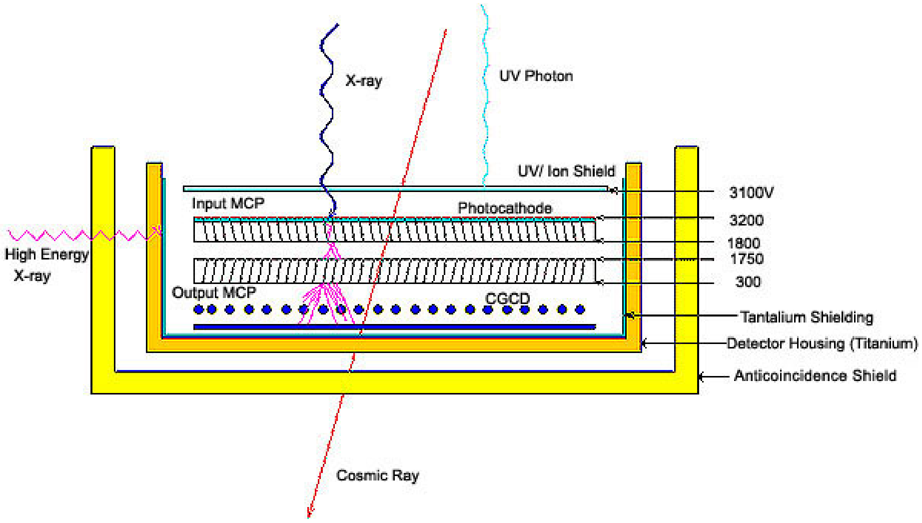

Figure 2.5: The *Chandra* High Resolution Camera (HRC).

Focal-plane arrays:	I-array	4 CCDs placed tangent to the focal surface
	S-array	6 CCDs in a linear array tangent to the grating Rowland circle
CCD format		1024 by 1024 pixels
Pixel size		0.4920 ± 0.0001 arcsec (23.985 microns)
Effective area (on-axis, cm^2)	@0.5 keV	110
	@1.0 keV	615
	@6.0 keV	205
Spatial resolution		$< 1''.0$
Field of View		$16' \times 16'$

Table 2.2: *Chandra* telescope parameters

2.4.1.2 ACIS

Advanced CCD Imaging Spectrometer (ACIS) contains 10 planar, 1024×1024 pixel CCDs captures high-resolution images and good-resolution spectra. Moreover, in conjunction with the High Energy Transmission Grating or Low Energy Transmission Grating, it can be used to obtain high-resolution spectra as well. In order to extend the response to energies lower than that are accessible by Front-Illuminated (FI) chips, two of the ten CCDs are Back-Illuminated (BI).

2.4.1.3 High resolution spectrometers

The *Chandra* suite of science instruments contains two transmission gratings—High Energy Transmission Grating (HETG) and Low Energy Transmission Grating (LETG), dedicated to high resolution spectroscopy. When operated with ACIS-S, HETG forms the High Energy Transmission Grating Spectrometer (HETGS) with a resolving power (E/ΔE) up to 1000 in the band 0.4–10 keV. The LETG, when operated with the HRC-S, forms the Low Energy Transmission Grating Spectrometer (LETGS). The LETGS provides the highest spectral resolution on *Chandra* at low (0.08–0.2 keV) energies.

2.4.2 Comparison between XMM and *Chandra*

XMM telescope was designed to complement the capabilities of *Chandra*. *Chandra*'s high-resolution cameras produce sharp images of discrete astronomical X-ray sources. The combination of high resolution, large collecting area, and sensitivity to higher energy X-rays makes it possible for *Chandra* to study extremely faint sources, sometimes strongly absorbed, in crowded fields. The grating spectrometers make it possible to do high resolution spectroscopy in the low energy regime (< 0.5 keV) as well as in the range >2 keV.

The extremely large collecting area of XMM provides very good S/N that allows us to do reliable detailed spectral analysis on a variety of X-ray sources such as galaxies, clusters, AGN and the diffuse X-ray background. The grating spectrometer (RGS) also allows for high resolution spectroscopy in the energy range $0.5 < E < 2$ keV. With its reasonably high sensitivity and spectral resolution, XMM is currently the instrument for the study of the DXB.

Observatory	**XMM-*Newton***			***Chandra***			
Detector	**EPIC MOS**	**EPIC PN**	**RGS**	**ACIS**	**HRC**	**HETG**	**LETG**
Energy range (keV)	0.15–15	0.15–15	0.33–2.5	0.1–10	0.1–10	0.6–10	0.16
Effective area (cm^2)							
@0.4keV	360	771	44	120	50		12
@1.0keV	922	1227	185	615	215	10	55
@6.0keV	768	-	-	205	45	25	20
Angular resolution (HEW)	$\sim 13''$	$\sim 15''$	-	$\sim 1''$	$\sim 0.5''$	-	-
Energy resolution (E/ΔE)	20–50	20–50	150–800	-	-	800–200	> 2000
Field of View	$30' \times 30'$	$30' \times 30'$	-	$16' \times 16'$	$31' \times 31'$	-	-

Table 2.3: Comparison of XMM and *Chandra* instruments

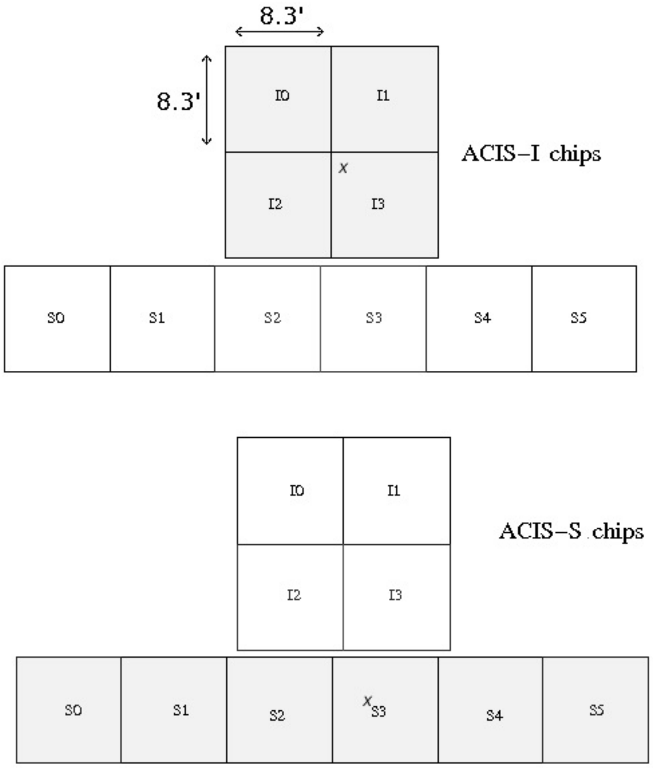

Figure 2.6: A schematic drawing of the ACIS focal plane, not to scale. The ACIS-I array consists of chips I0-I3 (shaded gray in the upper figure). The ACIS-S array consists of chips S0-S5 (shaded gray in the lower figure).

Chapter 3

Data reduction

3.1 Overview

The measurement and characterization of the cosmic X-ray background (CXB) has engaged the attention of astrophysicists for the past several decades. Since the pioneering X-ray experiment by Giacconi (Giacconi et al. 1962) to study X-ray emission from the moon with the serendipitous discovery of the diffuse X-ray background which was found to be isotropic and of extragalactic origin above $\sim$1 keV (Fabian et al. 1992) several experiments using rocket-borne instruments and satellite-mounted telescopes have revolutionized X-ray astronomy. An anisotropic diffuse Galactic component which is superposed on the isotropic background was also later discovered (Bowyer et al. 1968). All-sky surveys of the soft X-ray diffuse background in several bands from 0.1 to 6 keV (McCammon et al. 1983; Snowden et al. 1995) revealed that the diffuse X-ray background below $\sim$1.2 keV is made up of several distinct components with varying proportions in the different energy bands.

Analysis of the data from *HEAO-1* A-2 experiment showed that the X-ray spectrum in the range 3–50 keV could be well represented by a thin thermal Bremsstralung model with $kT \approx 40$ keV (Marshal et al. 1968). However, interpretation of the CMB spectrum from the COBE *FIRAS* instrument (Wright, 1994) showed that the density of any diffuse intergalactic medium hot enough to produce the observed diffuse X-ray background is two orders of magnitude too small to produce that background. Also, no significant Compton distortion was detected. It was soon realized that above $\sim$2 keV the CXB spectrum was well fit to a power law of the form $AE^{-\alpha}$ where A is a constant, E is the energy in keV and α is called the spectral index (Gorenstein et al. 1969). Deep focusing surveys with ROSAT to limiting fluxes of $\sim 10^{-15}$ ergs cm^{-2} s^{-1}

were able to resolve most of the soft CXB into discrete sources (e.g. Hasinger et al. 1998) the majority of which are thought to be active galactic nuclei and normal galaxies. Subsequent surveys with *ASCA* above 2 keV (e.g. Georgantopoulos et al. 1996); Ueda et al. 1998) and *Beppo*SAX (Gendreau et al. 1998) resolved more of the CXB in the hard band into point sources, mostly obscured and unobscured AGN lending support to the predictions of the population synthesis models based on unified AGN schemes (e.g. Madau et al. 1994; Comastri, 1995; Gilli, 2007). At the same time, at the faint end of the brightness scale there may be hiding new point as well as diffuse sources that are yet to be discovered.

With the superb sensitivity and angular resolution of *Chandra*, detection of point sources to very faint flux limits became possible. Deep *Chandra* surveys with long exposures have resolved most of the CXB above 1 keV into point sources, mostly AGN, revealing new fainter X-ray populations, such as obscured AGN and passive galaxies, and star-burst galaxies that had been poorly sampled in the past, giving large source samples that allow us to make valid statistical inferences about extragalactic sources which produce the cosmic background. Below $\sim$1 keV, the CXB is much more than a simple extrapolation of the power law can account for. Instead it is a complex blend of several components, discrete as well as diffuse (Kuntz et al. 2000). The uncertainty in the measurements of the absolute CXB has hampered the determination of its distinct components with a high degree of precision as well as their characterization. With the availability of large source samples along with long exposure times ($\sim$4 Ms) it has become possible to make more accurate measurements of the CXB and obtain better constraints on the CXB parameters. An absolute measurement of the CXB was undertaken by Hickox and Markevitch (Hickox et al. 2006, hereafter HM06), using the *Chandra* 2 and 1 Ms exposures, respectively, of the *Chandra* Deep Field North (Brandt et al. 2001) and the *Chandra* Deep Field South (Rosati et al. 2002). Improved statistics resulting from large exposure times and a more comprehensive source catalog make it possible to draw more reliable inferences on the composition of the CXB.

The first step in trying to characterize the CXB is the selection of the appropriate average aim-point and the observations. The *Chandra* Deep Field-North (CDF-N) and *Chandra* Deep Field-South (CDF-S) are the two deepest *Chandra* surveys (see Xue et al. 2011), each covering ∼440 square arcmins with enormous multi-wavelength observational investments. We chose the *Chandra* Deep Field South (CDFS) 4 Ms survey, one of the deepest sky surveys undertaken since the first 1 Ms CDFS probe (Giacconi et al. 2002), with a sensitivity limit of 9.1×10^{-18} ergs cm^{-2} s^{-1} in the soft band and having the highest source density of all surveys. The CDFS also has the deepest XMM-*Newton* survey (XMM-CDFS) with a nominal exposure time of 3.45 Ms (Ranalli et al. 2013) from 33 observations which have been used in our investigation. The *Chandra* Deep Field South is centered (average aim point) on $\alpha = 03^{\mathrm{h}}32^{\mathrm{m}}28^{\mathrm{s}}.06$, $\delta = -27^{\circ}48^{'}26^{''}.4$ (J2000). This direction has low Galactic neutral hydrogen column density ($\mathrm{N_H} \simeq 0.0088 \times 10^{22}$ cm^{-2}), no bright features or stars, has multi-wavelength coverage (optical, IR and radio wavelengths) and a large number of available spectroscopic and optometric redshifts. Moreover, one can build on the previous source catalogs with greater sensitivity and minimal source confusion.

Multi-wavelength identifications of X-ray sources detected in ultra-deep surveys are important to exclude spurious detections (Luo et al. 2010) as well as carry on follow up investigations. To study their cosmological evolution, their redshift determination is also essential. Panchromatic surveys such as the VLA radio (e.g., Kellermann et al. 2008), Spitzer IR (e.g., Damen et al. 2010), NIR K-band (e.g., Grazian et al. 2006), and GALEX UV (e.g., Morrissey et al. 2005) are available. The 740 sources used for our data reduction have been identified after extensive detection procedures with a binomial-probability source-selection criterion of $\mathrm{P} < 0.004$, and source-matching using seven ONIR (Optical/Near IR/IR/Radio) catalogs.

We used the resources offered by both the *Chandra* 4 Ms survey as well as the XMM-CDFS survey.. While *Chandra* has the highest sensitivity and resolution at the survey flux limit plus minimum source confusion, its effective area drops off sharply at energies >5 keV. XMM-*Newton* has larger photon collecting area in a broader energy range (0.5–8 keV) providing high S/N thus allowing good quality spectroscopy.

For our investigation of the cosmic soft X-ray background we make use of 33 XMM-*Newton* observations of the CDFS with a nominal exposure time of 3.45 Ms to study the diffuse X-ray background in the energy range 0.5–8 keV. Here we exploit the large effective area of the XMM-*Newton* telescope coupled with its reasonably good angular and spectral resolution to make an accurate determination of the spectral properties of the CXB and to derive its parameters and calculate intensities in several bands in the range 0.5–8 keV.

ObsID	Date	Exposure (ks)	RA (deg)	Dec (deg)
0108060401	2001-07-27	13.86843	53.0812	-27.7929
0108060501	2001-07-27	27.25446	53.0919	-27.7981
0108060601	2002-01-13	36.29391	53.1457	-27.8252
0108060701	2002-01-14	58.00492	53.1406	-27.8218
0108061801	2002-01-16	30.10377	53.1450	-27.8195
0108061901	2002-01-17	33.03461	53.1456	-27.8133
0108062101	2002-01-20	34.72473	53.1511	-27.8168
0108062301	2002-01-23	57.36402	53.1462	-27.8147
0555780101	2008-07-05	50.24151	53.1476	-27.7368
0555780201	2008-07-07	55.55344	53.1488	-27.7457
0555780301	2008-07-09	62.10838	53.1387	-27.7448
0555780401	2008-07-11	41.10292	53.1385	-27.7371
0555780501	2009-01-06	70.01074	53.1325	-27.8371
0555780601	2009-01-10	57.27154	53.1343	-27.8439
0555780701	2009-01-12	73.33367	53.1322	-27.8545
0555780801	2009-01-16	56.64329	53.1233	-27.8359
0555780901	2009-01-18	56.06108	53.1230	-27.8445
0555781001	2009-01-22	73.18634	53.1234	-27.8528
0555782301	2009-01-24	63.86822	53.1235	-27.8531
0604960101	2009-07-27	61.56630	53.1486	-27.7447
0604960201	2009-07-17	43.79502	53.1404	-27.7448
0604960301	2009-07-05	56.04061	53.1496	-27.7550
0604960401	2009-07-29	67.37832	53.1393	-27.7544
0604960501	2010-01-18	37.04331	53.1307	-27.8384
0604960601	2010-01-26	52.06067	53.1312	-27.8463
0604960701	2010-01-12	40.65510	53.1224	-27.8388
0604960801	2010-02-05	58.59998	53.1315	-27.8569
0604960901	2010-02-11	58.38064	53.1221	-27.8573
0604961001	2010-02-13	69.60476	53.1211	-27.8476
0604961101	2010-01-04	78.94026	53.1316	-27.8301
0604961201	2010-01-08	67.73826	53.1197	-27.8294
0604961801	2010-02-17	68.65162	53.1213	-27.8474

Table 3.1: CDFS-XMM exposures used for spectral analysis

3.2 Data reduction

Thirty three XMM-*Newton* observations of the CDFS (e.g. Ranalli, 2013) were selected for the analysis. We left out one observation with a low exposure because it was found to be not useful for the analysis. Table 3.1 lists the thirty two observations with their numbers, dates and exposures which correspond to cleaned and filtered time intervals, and the coordinates RA and Dec in EME2000. In our investigation, for the removal of point sources, we used the catalog of 740 point sources detected by one of the deepest ever cosmological surveys in the *Chandra* Deep Field South (CDFS) with a total exposure time of ∼4 Ms (e.g. Lehmer, 2012), allowing us to exclude point sources down to the lowest possible flux level and thus enabling us to not only carry out an absolute measurement of the unresolved cosmic X-ray background but obtain excellent statistics, with ∼100 Ks of good observing time per observation.

3.2.1 Data preparation

We used the Scientific Analysis Software[2] and the XMM-*Newton* Extended Analysis Software (*XMM-ESAS*, Kuntz & Snowden 2014, version 5.9) for data filtering and cleaning. To begin with, we chose the data from the EPIC-pn camera and used the scripts `epchain` and `pnfilter` to derive the clean filtered event lists. This ensured that the most recent versions of the CCF files and SAS software were used.

To filter the data of soft proton (SP) flares, the SAS task `espfilt` is used which creates diagnostic files and provides the necessary light curve cleaning. It creates two light curves—one for the FOV and the other for the corner region—and constructs a high energy count rate histogram for the FOV data. In the case where the time intervals are unaffected or only minimally affected by SP contamination, a Gaussian is fit to the peak with a 1.5 sigma upper and lower thresholds. Finally, it creates the GTI file for the good time intervals with count rates within the thresholds and filters the data using the `evselect` task. It should be noted this procedure removes only the obvious contamination where the count rate is significantly higher than the nominal

---

[2] SAS version -1.2, SAS release: xmmsas_20131209_1901-13.5.0

count rate. The diagnostic QDP plots were examined to get an idea of the extent of any possible SP contamination. In this case the asymmetry of the peak in the count rate histogram and its strong high count-rate tail implies that there is going to be residual soft proton contamination. Evidence of any residual SP contamination was looked for by running the tasks `proton-scale` and `proton`. From our analysis it was found that SP contamination was minimal.

3.2.2 Excision of point sources

The procedure adopted in the removal of point sources and diffuse sources is different from the one described in the *XMM-ESAS* manual. The `cheese` script in the *XMM-ESAS* makes the necessary masks and sources lists that will be used to create source-excluded spectra and images. Because of the large number of sources (∼740) that were to be removed, which SAS tasks cannot handle at one go, we had to create an external source list in terms of region files in both detector and sky coordinates. We created our own region fits files and used them to exclude all the sources. The XMM sources and the extended sources were completely masked using radii given in the catalogs. For the *Chandra* sources, choice of the right cut-out radius had to be done judiciously. We decided on the choice of $16''$ (half energy width (HEW) of the PSF) as the on-axis cutout diameter for *Chandra* point sources. This ensured that sufficient statistics were available for the estimation of the cosmic background. Thus half the contribution from the sources identified by *Chandra*, but not by XMM, would be left along with the truly diffuse emission. We later verified that the power law norm due to the *Chandra* sources within the HEW is had a value equal to that of the diffuse background within 1σ error.

To mask the sources, region list files in fits format in both detector and sky coordinates were created. Additional region selection from the full FOV can be done by including the appropriate region file in the filter expression. We limited our analysis to the *Chandra* exposure region to include all the *Chandra*-detected sources. A polygonal region in the XMM event map, that encloses the *Chandra* FOV, is chosen whose perimeter corresponds to ∼30 percent of the maximum exposure thus excluding the region outside the polygon where the large off-axis angles introduce greater uncertainty in determining the PSF. Around each point source a circular exclusion region is defined. Based on a linear relationship between small off-axis angles and the corresponding PSFs the the exclusion radii are calculated according to the formula

$$r = \frac{1}{2} \times \text{HEW} + k * \theta \tag{3.1}$$

where HEW is the half energy width in arc seconds, k =1.08 arcsec-arcmin^{-1} and θ is the off-axis angle in arc minutes.

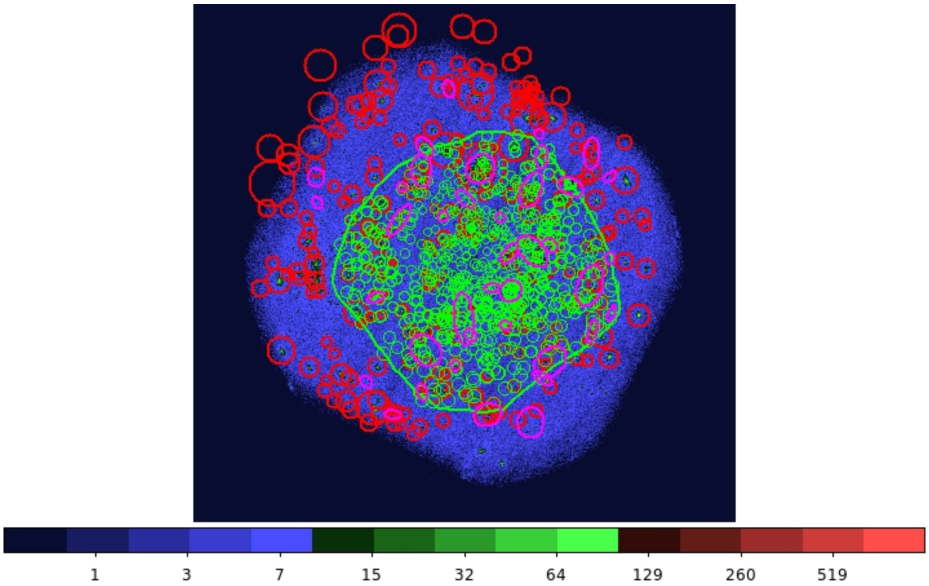

Figure 3.1: Point source exclusion regions overlaid on the CDFS map. Green circles represent *Chandra* regions with ≥30% of the maximum exposure, enclosed by the polygon. Red cirlces denote XMM source exclusion regions and magenta regions (ellipses) correspond to diffuse source exclusion regions.

3.3 Instrumental background

A major component of the total detected flux is the particle background due to instrument electronics and the fluorescent lines from the detector housing. An precise estimation of the instrumental background spectrum is critical to the measurement of the absolute CXB. This is achieved in the task `pnspectra` which creates not only a model quiescent particle background spectrum for user-defined regions of the detector, but also produces background subtracted and exposure-corrected images. To estimate the quiescent particle background (QPB), spectral extraction is done quadrant by quadrant for both normal and out-of-time (OOT) events. Since the QPB is temporally and spatially variable, the procedure needs to use the unexposed-region data (corner data) from a given observation together with data from archived observations as well as filter wheel closed data (FWC) from both the FOV and the unexposed region, to construct the appropriate QPB for that observation. An accurate estimation of the QPB is made by the ESAS tasks which also produce the area and exposure-normalized OOT-subtracted spectrum. Figure 3.2 shows the exposure-corrected, particle background-subtracted image of the CXB.

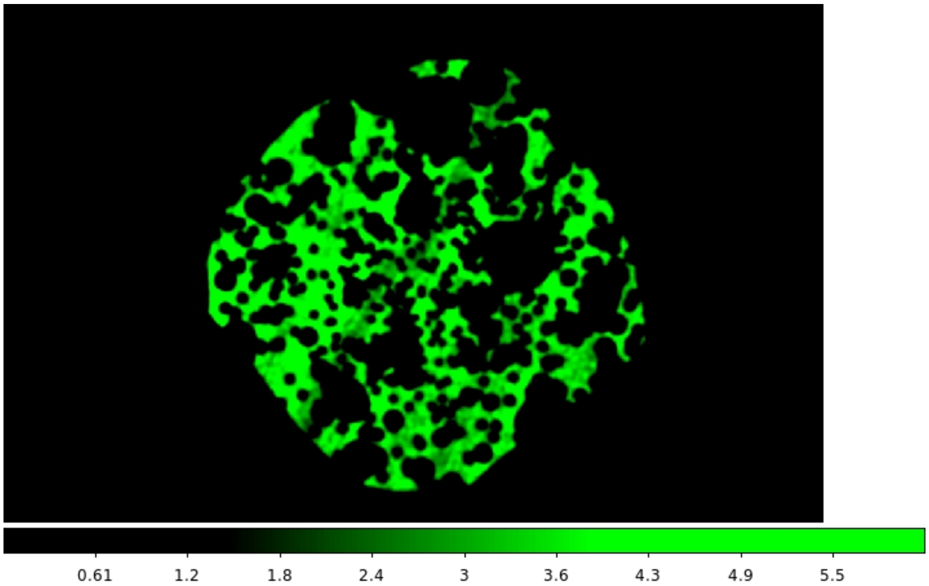

Figure 3.2: Unresolved Cosmic X-ray Background map from the CDFS derived using XMM-*Newton* data.

Chapter 4

Measurement of the unresolved Cosmic X-ray Background

4.1 Extraction of the spectrum

The next step in the process is to extract the selected FOV region from the observation data into a spectral file for each observation using the region filters and the standard filter expression for pn data. We used the ESAS script `pn-spectra` for spectral extraction.

The task of extracting the spectra works best when the source coordinates are in detector format. Many of the SAS tasks require detector coordinates for them to function properly. For the visual analysis of the background in the selected band and region of the field of view (FOV) it is necessary to generate images in both sky and detector coordinates. Images may be generated for standard events as well as OOT events. Since many of the tasks called by `pn-spectra` make use of detector coordinates, region masks need to be generated in detector coordinates. In particular, the ESAS script `pn-spectra` makes use of detector coordinates for spectral extraction. Using the routine `eskytodet` the sky coordinates were converted to detector coordinates before they could be used to make the masks in detector coordinates.

The cleaned and SP-filtered spectrum includes the OOT events spectrum, the sky background (cosmic diffuse X-ray background), and the detector background. Spectral extraction is done for both normal and OOT events and a scaled spectrum of the OOT events will be subtracted from the total background in the ESAS task. In both runs, the BACKSCAL which gives the scaled area of the region of spectral extraction is calculated. This is followed by `rmfgen` which generates the redistribution matrix (RMF) to be used along with the ARF (the ancillary response file) to estimate the instrument response. The task `arfgen` calculates the energy-dependent effective

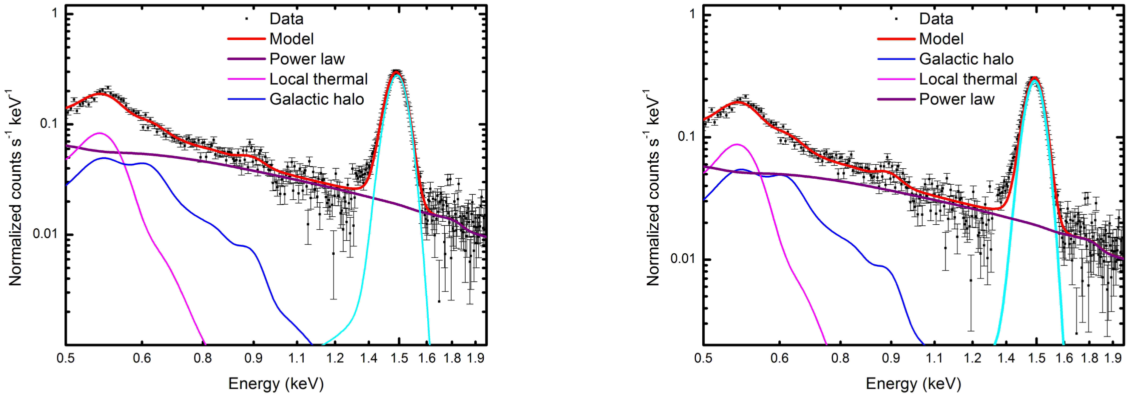

(a)

(b)

Figure 4.1: (a) Unresolved background-subtracted spectrum for the XMM-CDFS PN data. The simultaneous fit was done in the energy range 0.5–7.0 keV after removing the Al instrumental line (1.34–1.75 keV). (b) The same spectrum fit to the composite data from 32 observations.

area of the detector and writes it to ARF. Our analysis assumes that the unresolved sky brightness is uniform and the exposures have the same sky coverages since the pointings have essentially the same reference coordinates.

4.2 Results

We derived the composite spectra of the unresolved CXB for the thirty two data sets using `XSPEC`[3]. The results are shown in Figure 4.1. Even though the target observed is essentially the same the response matrix can change. Moreover, the data are taken from a ten-year period that spans one solar cycle which means time-varying components can significantly contaminate the spectra. Since we selected the data with the secondary goal of analyzing Solar Wind Charge eXchange (SWCX) (Cravens et al. 2000), instead of simply adding up the spectra of the thirty two observations we performed a simultaneous fit of the 32 datasets, thus obtaining tighter constraints and, at the same time, enabling an analysis of the temporal variance of SWCX. We used a simple model consisting of three additive components and one multiplicative compo-

---

[3] XSPEC version: 12.8.2; http://heasarc/gsfc/nasa.gov/docs/xanadu/xspec

nent: a thin-thermal unabsorbed plasma component modeled using APEC[4] (Smith et al. 2001) to account for the flux from the Local Bubble, a second thermal component absorbed by interstellar gas in the Galactic disc (Galactic halo emission) and an absorbed power law component to model unresolved extragalactic point sources (Seyfert galaxies, quasars and normal galaxies). In the simple three-component model we ignore the possible contribution from the time-varying component (SWCX) the analysis of which requires a detailed look at all the individual observations and the possibility of charge exchange contamination after looking at the fit results. A discussion of the SWCX contamination is given in section 7. A Galactic absorbing column density (Dickey et al. 1990) of 0.0088×10^{22} cm^{-2} was used for the absorbed components. Solar relative metal abundances (Anders et al. 1989) were chosen for the analysis to facilitate comparison with other studies.

The best fit parameters are given in Table 4.1. The errors quoted in this work are 90% confidence limits. We used an upper cut-off of 7.0 keV and lower cut-off of 0.45 keV for the fit, thus excluding strong instrumental lines such as those of Cu and also the strong low energy tail due to detector noise. Also excluded for the fit were the bins between 1.34 and 1.75 to avoid the Al Kα instrumental line. We were able to obtain a robust fit linking all the parameters. We also performed the fit by adding up all the thirty two spectra using **mathpha** and the results from both fits are in excellent agreement. The extragalactic parameters for the CDFS are consistent with those of HM06 within the 2σ limits.

4.3 Verification

We investigated the possible dependence of our results on the method of background subtraction and the spatial and temporal filtering that we adopted. Since we have a very good estimate of the particle background calculated using the standard ESAS tools the spectrum after background subtraction quantifies the absolute CXB to a high degree of precision within statistical and systematic errors. The region filtering was

---

[4] the ATOMDB code v2.0.2

Parameter	Simultaneous fit	Cumulative fit
Unabsorbed plasma component:		
Temperature (keV)	$0.089^{+0.015}_{-0.012}$	0.09 ± 0.01
Temperature (Kelvin)	$1.035^{+0.136}_{-0.171} \times 10^6$	$1.039^{+0.104}_{-0.119} \times 10^6$
Emission Measure ($\mathrm{cm}^{-6}\mathrm{pc}$)	$0.011^{+0.012}_{-0.0048}$	$0.0114^{+0.0093}_{-0.0049}$
Absorbed plasma component:		
Temperature (keV)	$0.218^{+0.012}_{-0.026}$	$0.229^{+0.013}_{-0.012}$
Temperature (Kelvin)	$2.51^{+0.142}_{-0.296} \times 10^6$	$2.66^{+0.15}_{-0.13} \times 10^6$
Emission Measure ($\mathrm{cm}^{-6}\mathrm{pc}$)	$0.00095^{+0.0004}_{-0.00012}$	$0.00093^{+0.00013}_{-0.00013}$
$\mathrm{N_H}(\mathrm{cm}^{-2})$	0.0088×10^{22}	
Absorbed power law:		
Normalization[a]	$4.73^{+0.15}_{-0.16}$	$4.50^{+0.17}_{-0.17}$
Power-law Γ	$1.89^{+0.058}_{-0.058}$	$1.81^{+0.064}_{-0.063}$
χ^2/**dof**	33305.11/32973	

[a] Units are photons s^{-1} keV^{-1} cm^{-2} sr^{-1}

Table 4.1: Model parameters of fits to CXB XMM cumulative spectra

done using the most comprehensive source catalog available which includes sources at the faintest flux level probed by *Chandra*. Additionally, XMM sources as well as ∼40 extended sources were also masked out. In order to minimize the uncertainties introduced by too low exposure times, and the increased PSF widths and asymmetry at larger off-axis angles, we only used the region centered around the aim point bounded by a polygon whose points correspond to a lower threshold of ∼30% of the maximum *Chandra* exposure.

A possible contamination from soft proton flares can affect the results. As was pointed out in section 2, `pnfilter` removes only the obvious SP contamination with count rates significantly above the nominal level. We carefully looked at the diagnostic QDP files showing the light curves of the 32 data sets and found that the residual flare was minimal. However, to make sure that our results are not impacted by this component we added a power law component, not folded through the instrument response, to our four-component model and fitted the data. The contribution from this component was found to be negligible for any reasonable choice of the power law index, and the fit results were unaffected. We concluded that any significant SP flare contamination was nearly non-existent. In estimating the SXRB, another possible contaminant is the temporally variable component due to Solar Wind Charge Exchange (SWCX). The 32 observations, centered around (RA_PNT=53°.1465, DEC_PNT=−27°.7374) were chosen in such a way that these are less affected by SWCX (Henely 2010). Strong enhancements in Oxygen line intensities indicate SWCX emission. The presently available practical method to estimate SWCX is to analyze temporally separated multiple observations of the same target and study the variations in the Oxygen line intensities. Enhancements in O VII and O VIII line intensities can be used to constrain models of SWCX emission (Henley 2010). In this study, the oxygen line intensities of the thirty two observations were derived, a detailed analysis of which is given in the section 7.1.

4.4 Contamination from SWCX

X-ray emission resulting from the interaction of highly ionized atoms in the solar wind with neutral atoms, such as H and He in the inter stellar medium (ISM), has been recognized as a major contributor to the foreground diffuse X-ray flux. Evidence of a time-varying component in the diffuse emission was detected in the ROSAT all-sky survey (Snowden et al. 1995) as long term enhancements (LTE) which had been found to be generally correlated with strong solar wind variations (Freyberg 1994). Cox (1998a) suggested that charge exchange (CX) can occur between ions and neutrals both in the heliosphere (heliospheric emission) and in the exosphere (geocoronal emission).

A charge exchange reaction may be represented by the following relations:

$$\mathrm{A^{+n} + H\ [He] \Rightarrow A^{+(n-1)*} + H^{+1}\ [He^{+1}]} \tag{4.1}$$

$$\mathrm{A^{+(n-1)*} + H^{+1}\ [He^{+1}] \Rightarrow A^{+(n-1)} + H^{+1}\ [He^{+1}]} + h\nu \tag{4.2}$$

Here A refers to any of the solar wind ions, A^* denotes the excited state of the charge-exchanging ion, H is neutral hydrogen and He is the neutral helium. Highly charged ions like O vii and O viii strip electrons from interstellar and geocoronal neutrals, enter an excited state and, in the process of de-excitation, emit photons in the EUV or X-ray energy range.

Even though an accurate determination of the amount of SWCX emission is beset with several challenges, not only because of its wide variation with time and viewing geometry but also because of the uncertainties in measurements of the relative abundances, densities and velocities of the ions, it is possible to obtain reasonable constraints on the contributions of the most important *Chandra* and XMM-detectable CX ions—O vii and O viii—and deduce the extent of SWCX contamination in the diffuse emission in the specific direction being investigated. The SWCX continuum spectrum is made up of the same emission lines as those of the LB and the halo, and so, even though its spectral structure is different it is not easy to disentangle their distinct contributions to the CXB because of the limited CCD resolution of the XMM detectors. At the same time, it is important to determine the relative contributions of the LB, the halo and the SWCX to the SXRB in order to characterize the total observed diffuse X-ray spectrum and assign meaningful constraints to other truly diffuse non-local components.

In this section we explore two slightly complex models to analyze SWCX contamination of the CXB illustrating its temporal variation with the solar cycle phase and show that the CXB parameters already derived in section 5 are largely model-independent.

4.4.1 Gaussian lines SWCX model

The Gaussian Lines SWCX (two-gaussian) model is a modified form of the three-component model to which two δ functions of zero width at 0.57 keV and 0.65 keV are added to model the O vii triplet and O viii lines respectively, and their amplitudes are the exposure-weighted averages of intensities in LU. The LB is modeled using APEC thermal plasma model (Smith 2001) with solar abundances, so that the intensities in LU due to the δ functions represent SWCX. Yet another modification of this model is one in which an additional δ function is included to model the Ne ix ion (0.92 keV)

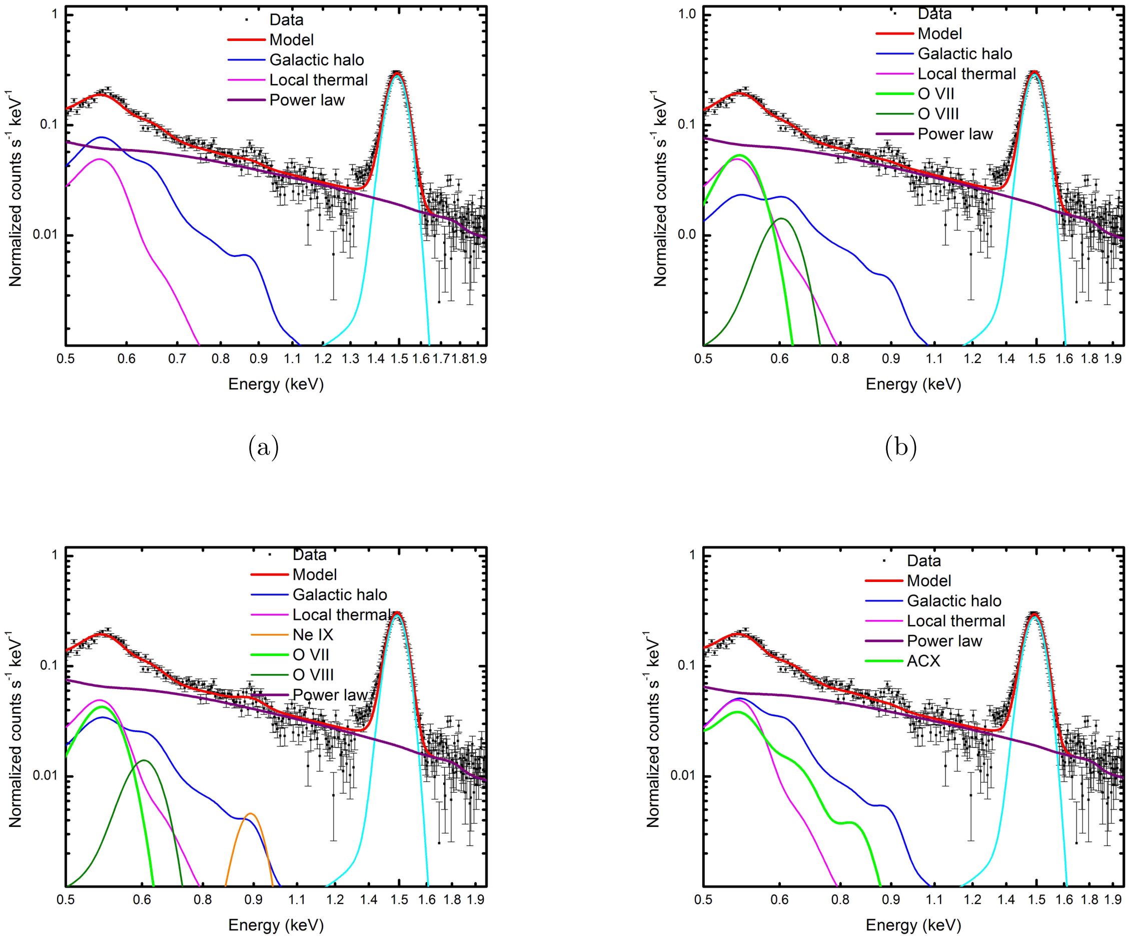

(a) (b)

(c) (d)

Figure 4.2: (a) The simple model (SM-II) with the LB parameters frozen. (b) The Two-gaussian model in which the δ functions represent O VII and O VIII. (c) The Three-gaussian model with the Ne IX line in addition to the oxygen lines. (d) The ACX model.

which was found to be significant (see section 4.5.2). The widths and the energies are frozen and the normalizations of the O vii and O viii are allowed to vary. The temperature of the Local Bubble, independently determined from the ROSAT data (Liu et al. 2016) as well as the emission measure were frozen. A simultaneous fit was done for the thirty two datasets with all the parameters tied except for the normalizations of the gaussian lines. This is justified because the LHB and the halo parameters are not expected to show any significant temporal variation, the pointing directions being essentially the same.

Figure 4.2 shows the composite spectra with the model and the various components. The fit results are shown in table 4.2. The delta functions track the variation in SWCX emission over a period of ∼nine years from July 2001 through February 2010. Their amplitudes show enhancements during periods of high solar activity. In particular, for the observation 0108061901 taken in 2002, a period of solar maximum, the O vii line intensity jumps to as much as three times its average value of ∼0.9 LU during the solar cycle demonstrating the correlation between elevated solar activity and SWCX enhancements. The average value of ∼0.9 LU for the solar cycle phase is of the same order (Cravens 2000) as the LHB O vii line intensity of ∼1.0 LU. The average O viii intensity is ∼0.3 LU giving a O viii/O vii ratio of 0.333 which, as shown in section 4.5.1, agrees within error bars, with the slope (0.343) of the linear best fit to O viii-O vii line intensities.

The fit is good with a χ^2 value of 32568.73 for 32911 degrees of freedom. The halo norm in this case gets lower than the average value of 0.00088 cm^{-6}pc, still within the 2σ limit, thereby slightly overestimating the halo temperature which is expected from their functional relationship. Considering the significance of the Ne ix line which, as much as it is a diagnostic of astrophysical plasma, could contribute to SWCX in the high temperature regime, the model was modified by adding a δ function at 0.92 keV. The resulting model is named the three-gaussian model in the table 4.2 for comparison.

4.4.2 The ACX model

The ACX (ATOMDB Charge eXchange) model is an approximate model used to study the CX capture of an electron from a donor (neutral H or He) by a receiving ion using several simplifying assumptions (Smith et al. 2014a). The model uses relative cross sections to calculate relative rates of capture into a peak $n^{'}$ shell making use of the energies and transition probabilities between these levels taken from the ATOMDB database version 2.0.2 (Foster et al. 2012). The distribution of the electron among the various angular momentum states is governed by the *Separable* weighting function (see Smith 2014a for details). The ACX model used to study SWCX assumes that each ion undergoes only a single CX in the line of sight. This option is selected by setting the flag **swcx** $= 1$. Also the **model** flag is set to 8, which means not only that if the most probable n shell for electron capture is not an integer the captured electrons are distributed between the two nearest n shells, but also that the *Separable* function is chosen.

We used the ACX-SWCX model to do a simultaneous fit to the 32 datasets by linking all the parameters except the norm. We froze the SWCX parameters to their recommended values: FracHe0 (0.090909), abundance (Anders & Grevesse solar values), redshift (zero), **swcx** (1) and **model** (8) (see Smith et al. 2014b). In addition, we also fixed the temperature and the norm of the local bubble for the pointing calculated from ROSAT data (Liu et al. 2016) and allowed all other parameters to vary. The local bubble, halo and power law models give values that are consistent with those of the simple models at the 90% confidence level. While the assumption of an ion population in collisional equilibrium determined by a single temperature is not realistic, the ACX norms provide a fairly good estimate of the extent of the SWCX contamination. Since the ACX model does not take into account the actual CX cross sections and relies on approximate estimates of the ion densities, the ACX norms only give a scaled emissivity of the charge exchanging plasma. As figure 4.3(b) shows, the ACX norms are correlated with the the O VII line intensities.

Parameter	SM-I[a]	SM-II[b]	Two-gaussian model[c]	Three-gaussian model[d]	ACX[e]model	Galeazzi	McCammon	Markevitch
Unabsorbed plasma component:								
Temperature (keV)	$0.089^{+0.012}_{-0.015}$	0.099	0.099	0.099	0.099	0.095	0.099	-
Temperature (Kelvin)	$1.04^{+0.14}_{-0.17} \times 10^6$	1.15×10^6	1.15×10^6	1.15×10^6	1.15×10^6	1.11×10^6	1.15×10^6	-
Emission Measure ($cm^{-6}pc$)	$0.011^{+0.012}_{-0.005}$	0.0036	0.0036	0.0036	0.0036	0.0082	0.0088	-
Absorbed plasma component:								
Temperature (keV)	$0.22^{+0.012}_{-0.026}$	$0.184^{+0.004}_{-0.004}$	$0.226^{+0.025}_{-0.034}$	$0.20^{+0.04}_{-0.012}$	$0.20^{+0.005}_{-0.005}$	0.191	0.225	-
Temperature (Kelvin)	$2.53^{+0.14}_{-0.296} \times 10^6$	$2.13^{+0.439}_{-0.443} \times 10^6$	$2.62^{+0.285}_{-0.396} \times 10^6$	$2.32^{+0.44}_{-0.14} \times 10^6$	$2.34^{+0.62}_{-0.56} \times 10^6$	2.27×10^6	2.62×10^6	-
Emission Measure ($cm^{-6}pc$)	$0.001^{+0.0004}_{-0.0001}$	$0.0014^{+0.0001}_{-0.0001}$	$0.00047^{+0.00026}_{-0.00012}$	$0.00064^{+0.00014}_{-0.00026}$	$0.0012^{+0.00007}_{-0.00007}$	0.0034	0.00097	-
N_H (cm^{-2})	0.0088×10^{22}	0.0088×10^{22}	0.0088×10^{22}	0.0088×10^{22}	0.0088×10^{22}	0.0088×10^{22}	0.018×10^{22}	-
Absorbed power law:								
Normalization[f]	$4.73^{+0.15}_{-0.16}$	$4.95^{+0.11}_{-0.11}$	$5.12^{+0.13}_{-0.13}$	$5.04^{+0.131}_{-0.129}$	$4.68^{+0.110}_{-0.113}$	14.8	12.3	3.3 ± 0.6
Power-law Γ	$1.89^{+0.058}_{-0.056}$	$1.96^{+0.046}_{-0.045}$	$2.05^{+0.050}_{-0.050}$	$2.04^{+0.052}_{-0.050}$	$1.84^{+0.043}_{-0.044}$	2.2	1.52	$1.84^{+0.48}_{-0.35}$
χ^2/dof	33305.11/32973	33315.89/32975	32568.73/32911	32554.57/32910	32667.04/32943	-	-	-

[a] This refers to the three-component model in which the Local Bubble parameters are not frozen.

[b] This model is the same as the above except that the LB parameters are frozen to their *ROSAT* data-derived values.

[c] This contains the lines O VII and O VIII modeled as δ functions, added to the simple model, SM-II.

[d] An additional gaussian at 0.92 keV is added to the two-gaussian model.

[e] The AtomDB charge exchange model by Smith et al. 2014b.

[f] Units are photons s^{-1} keV^{-1} cm^{-2} sr^{-1}

Table 4.2: Comparison of model parameters of fits to CXB XMM cumulative spectra

4.5 Analysis of results

The best fit values for the plasma parameters, in general, show good agreement with the values obtained by Mccammon et al. 2002 and Galeazzi et al. 2007 who used sky regions with similar column density and with all bright features removed. However, the power law normalizations are different because in addition to the bright sky features, we have efficiently removed all point sources down to the faintest flux at the level of $\sim 10^{-18}$ ergs s^{-1} cm^{-2}. We obtain a value of 4.825 photons s^{-1} keV^{-1} cm^{-2} sr^{-1} for the power law normalization which is consistent with the value of HM06 who uses a similar procedure for source exclusion.

We used the fit results to derive the electron densities and thermal pressures for the LHB and the Galactic halo assuming that the hydrogen and helium atoms are fully ionized. The equation for electron density is given by the relation, $n_e^2 = 1.225\ \mathrm{EM}/R$ where EM is the emission measure and R is the spatial extent of the plasma region. Thermal pressure is: $P_{\mathrm{th}} = 1.92\ n_e T$. For the Galactic halo using an average thickness of 3.25 kpc for the disc at an equilibrium temperature of 2.354 $\times 10^6$ K, the electron density and thermal pressure are found to be 0.000591 cm^{-3} and 2.671×10^3 cm^{-3} K respectively. Using an average radius of 100 pc for the LHB, with its frozen parameters, the electron density and thermal pressure p/k work out to be 0.00663 cm^{-3} and 1.4617×10^4 cm^{-3} K respectively. Our results are comparable to the values predicted by the models of Smith and Cox (Smith et al. 2001). These values are also consistent with the results obtained recently Galeazzi et al. (2007).

4.5.1 Comparison of the models

The DXB parameters were re-derived using the simple model with the LB parameters frozen to their ROSAT data-derived values for comparison with the SWCX models.

We refer to this modified simple model as SM-II. Despite the fact that ∼18% of our observations were drawn from the solar maximum phase, in general, the parameters do not seem to be significantly affected by SWCX emission in this direction if we go by SM-I except for the LB emission measure which has an error of 2 σ's. In SM-I (figure 4.1) we attribute all the foreground flux to the LB and the O vii/O viii lines ratio seems to be consistent with a halo temperature of ∼0.216 keV which is well within 1σ of 0.206 keV, the average over all the models. However, the LB EM is apparently high in comparison with the ROSAT data-derived value in this direction which implies there is a significant contribution from SWCX that is not handled by the baseline model. In SM-II, which also serves only a heuristic purpose, since both the LB emission measure and temperature are frozen the excess flux coming from SWCX is attributed to the halo as may be seen from figure 4.2(a). This is reflected in the halo temperature being lowered by ∼8% from the average value. While this is not too drastic for the halo temperature, it certainly does not depict the full picture given the potentially significant contamination due to SWCX .

In the gaussian models, the prominent ions responsible for SWCX emission were included as δ functions. Ideally all the SWCX ions should be included to accurately model SWCX. However, owing to the incomplete nature of the atomic data on charge exchanging plasma as well as the limited resolution of the CCD detectors, we could only model a few dominant lines. Considering that O vii and O viii constitute the dominant SWCX lines, this is not a serious constraint, and the results justify the model we have used. Figure 4.3(a) shows the linear best fit of the O vii vs O viii line intensities and the slope is 0.343.

A sophisticated approach to modeling SWCX is adopted by Smith et al. 2014 in their ACX model which was discussed in section 7.2. It is obvious that the ACX model while giving abundance-based weight to all SWCX ions gives a re-scaled measure of the oxygen line intensities and attributes the excess flux to the halo. This is to be expected given the fact that the model does not consider actual cross sections and relies on rough estimates of ion densities, both of which are critical when the temporal variations of SWCX are to be modeled. The ACX norms only give a scaled

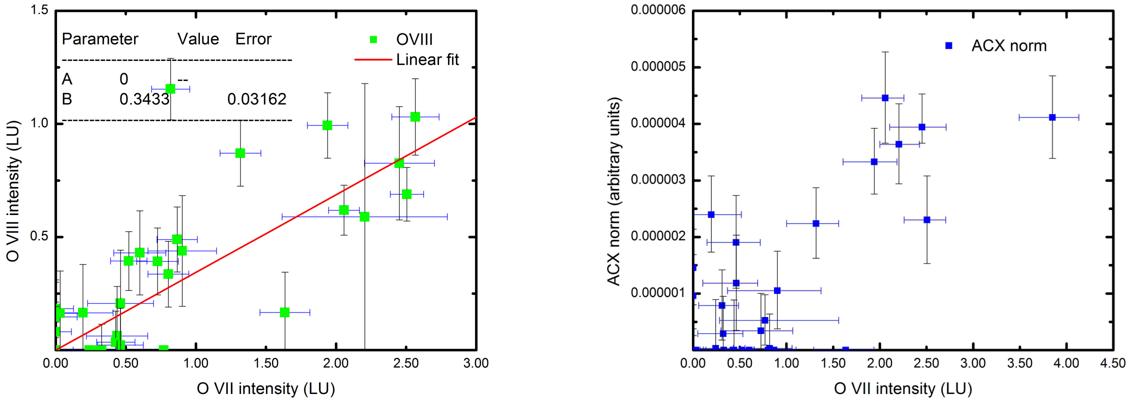

(a) (b)

Figure 4.3: (a) Linear fit to O vii and O viii correlation. (b) Variation of ACX norm (arbitrary units) vs O vii over one solar cycle.

emissivity of CX plasma. The model is an approximation that does not include the actual cross section of the charge exchange process itself, and so the norm has no physical use except as a relative scaling (see Smith et al. 2014). At the same time, as figure 4.4(b) shows, the model can be used as an excellent diagnostic tool to predict SWCX and to confirm the results from other models using correlation analysis. Since the model can treat SWCX for only a single presumed equilibrium temperature at a time rather than multiple temperatures, it has limitations when dealing with such wide swings in thermal conditions as exist in the solar corona. The ACX model can potentially be a powerful tool for characterizing SWCX if a multi-temperature treatment of the CX-ing plasma is accomplished along with the inclusion of an accurate treatment of CX cross sections. Fortunately for our purpose, such a sophisticated analysis of the SWCX was not required owing to the low degree of contamination. The simpler models—the gaussian models that we used—adequately explain and quantify the extent of CX contamination in our data reasonably well and serve to constrain the SXRB parameters to a high degree of accuracy. The gaussian models improve upon the simple models, and the O vii and O viii lines quantify the average SWCX contamination more or less accurately, in the CDFS over one solar cycle. Their relative normalizations represent, in principle, a measure of the temperature of the CX-ing plasma even though there is a large uncertainty in this owing to its non-equilibrium nature. While the two-gaussian model may not give a precise characterization of the halo parameters when compared against other models that include the relative contributions of all possible SWCX lines, it clearly highlights the significant contribution from SWCX that must be taken into account in estimating the DXB parameters.

4.5.2 Significance of the Ne IX line

As mentioned in section 4.4.1, after the fit was done, we noticed an excess at around 0.92 keV (the Ne IX). Therefore, we added another gaussian line with zero width and the gaussian energy frozen at 0.92 keV. This reduced the χ^2 by 14 for one additional degree of freedom. The Ne IX has an intensity of 0.081 ± 0.030 LU with a significance of more than 3 sigmas. This also resulted in an O VII/O VIII ratio on par with the ACX model. In fact the line ratios for the ACX model and the O VII-O VIII-Ne IX model agree within $\sim$2%.

Neon is an an astrophysically abundant element not affected by dust depletion, with emission lines around 1 keV that can be easily detected by both *Chandra* and XMM-*Newton*. He-like Neon is found in plasmas in CIE with temperatures in the range 5×10^5–10^7 K and thus, Ne IX can arise from all types of astrophysical sources.

We also looked at the temporal variation of the Ne IX line and did not notice any definite correlation with the Oxygen lines. Even though there may be some contribution from SWCX, the Ne IX line being another diagnostic of astrophysical plasma, can originate from the ISM as well as the halo of the Galaxy, thus exhibiting a higher than solar abundance.

4.5.3 Temporal variation of SWCX

Enhancements in the X-ray intensity over long time periods (spanning hours to several days) detected from ROSAT maps gave the first hints of a time-varying component in SXRB (Snowden et al. 1995). These long term enhancements (LTE) were later

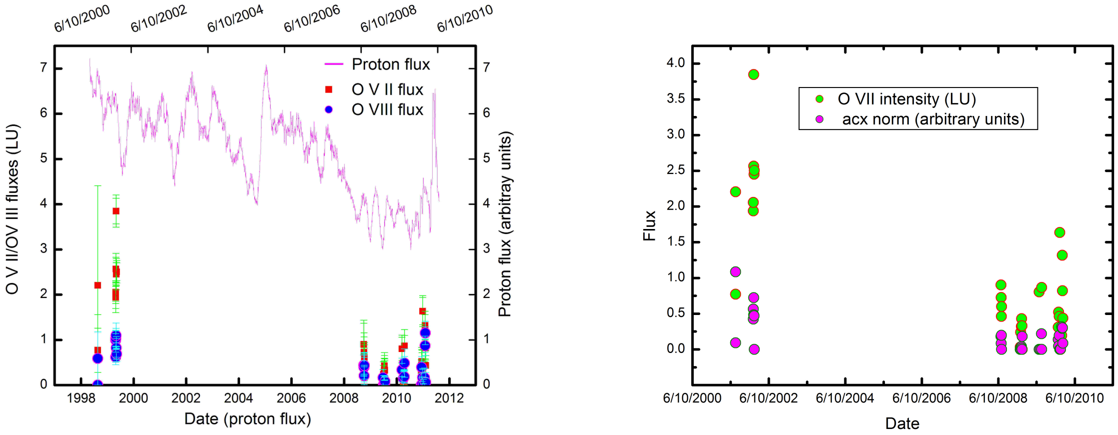

(a)

(b)

Figure 4.4: (a) Correlation of O vii and O viii fluxes (LU) with solar proton flux (arbitrary units). (b) Variation of ACX norm (arbitrary units) and O vii intensity over one solar cycle.

found to be correlated with extreme solar wind events such as coronal mass ejections (CME). The LTE's also imply an underlying quiescent component for the SWCX (Cravens 2000) which responds to the strong solar wind events by heightened levels of SWCX emission. Our data have been chosen from a nine-year period that spans a solar cycle starting with the solar maximum with the secondary goal of studying the temporal variation of SWCX. During solar maximum, up to three CME's can occur per day, that can be accompanied by solar flares, resulting in a sudden rise in solar wind flux which is reflected in a corresponding enhancement in the heliospheric SWCX emission. Extreme solar phenomena are characterized by temperatures of tens of millions of kelvin leading to the release of high charge state ions at heightened levels. The important solar wind ions producing SWCX emission are O^{+7} and O^{+8}. During solar maximum, the relative abundances of these ions can jump to higher levels leading to higher charge transfer reactions resulting in spurts of heliospheric X-ray intensities detectable near the Earth ∼4–7 days after the ions leave the Sun.

Figure 4.4(a) shows the variation of O vii and O viii intensities (LU) over several long term periods during the solar cycle phase (2001–2010). Solar proton fluxes (left Y-axis; month-averaged and in scaled units) calculated for several dates (lower X-axis) during the solar cycle are also shown. O VII and O VIII intensities (right Y-axis) were derived from data available for the dates shown (upper X-axis). The O VII and O VIII intensities are clearly correlated with the solar proton flux. This gives a quantitative measure of the temporal variation of SXRB that had been observed from the *ROSAT* data and was later explained as being associated with variations in the solar wind flux and ions composition, which correspond to the changing conditions in the active regions of the solar corona. A similar variation is found in the ACX norms (scaled units) over the solar cycle that are obviously correlated with the O VII line intensities (Figure 4.4(b) giving additional confirmation of our results. Thus the findings on the temporal variation of SWCX from the different models turn out to be consistent.

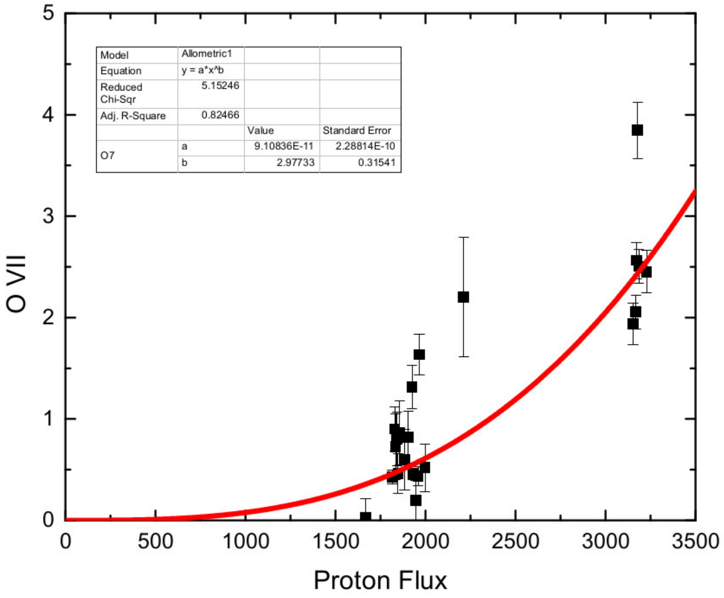

Model	Allometric1		
Equation	y = a*x^b		
Reduced Chi-Sqr	5.15246		
Adj. R-Square	0.82466		
		Value	Standard Error
O7	a	9.10836E-11	2.28814E-10
	b	2.97733	0.31541

Figure 4.5: Cubic fit to O VII intensity vs solar proton flux.

4.5.4 The unresolved Cosmic X-ray Background

Table 4.3 shows the unresolved CXB intensities for different bands. The observed fluxes were derived using an unabsorbed APEC plus absorbed APEC plus absorbed power law model.

From the time of the A-2 experiment of *HEAO 1* (Garmire et al.) it has been known that the extragalactic X-rays $\geq$1 keV could be approximated by a power law with spectral index $\Gamma \sim$1.4. However, the spectral index can vary over a wide range around this value depending on the hardness of the sample (Mushotzky et al. 2000) and the source-type. Distant star-forming and normal galaxies show spectral indices in the range of $\Gamma \sim$1.7–2.2. Therefore, for the absorbed power law fit we allowed both the normalization and the spectral index to vary since this was not found to make a significant difference to the value of the flux. HM06 used an unabsorbed power law to calculate extragalactic component in the bands 0.5–2 keV, 1–2 keV and 2–8 keV. In all the bands we get larger values for the intensities of the extragalactic component than those obtained by HM06. The fact that we get a higher power law norm for the unresolved background explains the larger value for the unresolved flux in the 0.5–2 keV band. Additionally, there is a significant contribution from the local thermal component modeled by absorbed APEC which is absent in HM06. The larger flux in the first two bands indicates a greater contribution from truly diffuse sources and unresolved point sources such as late-type star forming galaxies, obscured AGN, early-type galaxies and Galactic stars.

Adding the contributions from all the sources, except for the sources in the brightest group (flux $> 10^{-14}$ ergs cm^{-2} s^{-1}), to the unresolved intensity, we get 1.56×10^{-12} ergs s^{-1} cm^{-2} deg^{-2} for the total extragalactic intensity in the 1–2 keV band, and 4.09×10^{-11} ergs s^{-1} cm^{-2} deg^{-2} in the 2–8 keV band. This corresponds to a resolved fraction of 80% in the 1–2 keV band and 84% in the 2–8 keV band, and a power law normalization (for $\Gamma = 1.6$) of 11.38 ± 0.01photons cm^{-2} s^{-1} keV^{-1} sr^{-1} at 1 keV which is very close to the value obtained by De Luca and Molendi (2004). We also obtain a total flux of $(3.09 \pm 0.05) \times 10^{-12}$ ergs s^{-1} cm^{-2} deg^{-2} for the ROSAT 3/4 keV band which is consistent with the estimates obtained by Kuntz et al. (2001), Gupta et al. (2009a) and similar results based on XMM-*Newton, Chandra and Suzaku* observations.

4.5.5 New source populations and diffuse components

Extrapolation of $\log N$–$\log S$ curves for different point source populations to surface fluxes lower than the CDFS flux limit shows that the integrated intensities in the bands 1–2 keV and 2–8 keV are much lower than the observed intensities (e.g. L12, HM06). In the 1–2 keV band, both for AGNs and star-forming galaxies, the predicted intensities are much lower than the observed intensities which implies that if the CXB is entirely due to point sources, the $\log N$–$\log S$ curve will have to be steeper. In the hard band also, no single AGN or galaxy population can contribute all the observed flux. There is considerable uncertainty as to what types of point sources could account for all the observed flux. Contributions from exotic sources such as dark matter decay cannot be ruled out (e.g., Abazajian 2001). Star-forming galaxies—both low and high redshift—along with obscured and Compton-thick ($N_H > 10^{23}$ cm^{-2}) AGN provide the majority of the observed intensity in both bands. However, in the soft band, we expect a significant contribution from intergalactic gas in the warm-hot phase (WHIM). In fact, autocorrelation studies of the X-ray background indicate such a contribution and hydrodynamic simulations suggest that $\sim$12% ± 5% of the CXB in the < 1 keV regime is the WHIM flux (eg., Cen et al. 2006; Ursino et al. 2006; Galeazzi et al. 2009). Solar wind charge exchange makes an important contribution to the foreground emission, which, being highly temporally variant and look-direction dependent, is not easily quantified. However, using approximate models such as the ones used in section 7, we can obtain reasonably consistent estimates of the extent of contamination of the data.

4.6 Conclusion

We derived the cumulative spectrum of the diffuse cosmic X-ray background (CXB) using thirty two observations of the *Chandra* Deep Field South from the XMM-*Newton* public archive and made an absolute measurement of the unresolved X-ray flux of the cosmic soft diffuse X-ray background. The use of large statistics enabled the determination of the plasma parameters with tighter constraints. We made use of the standard ESAS routines in their original as well as modified forms to adapt them to our task. Point source exclusion was carried out using the up-to-date catalog based on the ultra-deep 4 Ms *Chandra* observation of the *Chandra* Deep Field South. The use of the ESAS package allowed a clean measurement and subtraction of the particle background enabling us to make a precise measurement of the diffuse X-ray background.

Total[1] (using apec plus absorbed (apec + power law))		
Energy band (keV)	This work	Markevitch
0.5–1	$2.915^{+0.0608}_{-0.0792}$	5.0 ± 0.4
0.5–2	$4.519^{+0.071}_{-0.092}$	6.0 ± 0.5
0.5–7	$8.153^{+0.0390}_{-0.0363}$	-
0.5–8	$8.612^{+0.0896}_{-0.0829}$	-
1–2	$1.604^{+0.042}_{-0.076}$	-
2–8	$4.099^{+0.0376}_{-0.0398}$	-
Extragalactic[2] (using absorbed power law)		
0.5–1	1.264	-
0.5–2	2.823	2.05 ± 0.41
1–2	1.559	1.2 ± 0.19
2–8	4.094	3.6 ± 2.2

[1,2] Intensities are in units of 10^{-12} erg s^{-1} cm^{-2} deg^{-2}

Table 4.3: Intensities of the unresolved CXB

We obtain significant CXB intensities due to extragalactic sources in the 1–2 keV energy range as well as in the 2–8 keV band. We get an unresolved intensity of $(4.52^{+0.0608}_{-0.0792}) \times 10^{-12}$ ergs cm^{-2} s^{-1} deg^{-2} in the 0.5–2 keV band. We also find unresolved extragalactic intensities of 1.559×10^{-12} ergs cm^{-2} s^{-1} deg^{-2} and 4.094×10^{-12} ergs cm^{-2} s^{-1} deg^{-2} in the 1–2 and 2–8 keV bands respectively. A difference of ∼2 sigmas for the 1–2 keV flux from the value obtained by Markevitch could point to the existence of some truly diffuse or unresolved sources such as groups and galaxy clusters or exotic sources yet to be discovered. The fact that extrapolation of the $\log N$–$\log S$ curve to lower flux limits does not exhaust the observed flux predicts the possible existence of fainter source populations as well as truly diffuse components that are not yet completely determined.

We started with a simple three-component model that consists of an unabsorbed *apec*, an absorbed *apec* and an absorbed power law using it as the base line model to analyze the diffuse cosmic X-ray background. We were able to obtain a robust fit to the data and derive the relevant parameters for the three dominant sources that produce the observed SXRB spectra—a thermal plasma in collisional equilibrium at a temperature of ∼0.099 keV in a cavity surrounding the Sun known as the Local Bubble, a hotter halo of gas surrounding the Galactic disc at an equilibrium temperature of ∼0.2 keV and an extragalactic component of unresolved point sources which are mostly AGNs and normal galaxies. The derived parameters are in general consistent with values determined in previous measurements. We also estimated the emission measures, electron densities and thermal pressures of the plasmas and the values agree with previous results. The value of the unresolved power law norm is consistent with the removal of all point and extended sources down to the lowest possible flux limit.

Having obtained the relevant model parameters, we extended the baseline model by adding to it two δ functions at the typical O VII and O VIII line energies—0.57 keV and 0.65 keV to analyze the contribution from the SWCX emission. We found clear evidence of a time varying component that significantly effects part of the soft diffuse emission. We also added another δ function after having noticed some excess flux at ∼0.92 keV (Ne IX) pointing to a more-than-solar abundance. This suggests that a precise measurement of the SXRB entails an accurate modeling of the important atomic lines that are responsible for the SWCX emission. We also employed a third, more complex model called the ACX model which can be used to obtain a very good estimate of the level of SWCX contamination. We found that, in general, all the three models produced consistent results as far as the diffuse CXB parameters are concerned.

Chapter 5

Extra-Galactic resolved sources

5.1 Perspective

The Cosmic X-ray Background (CXB) is predominantly composed of the X-ray emission from faint discrete sources. The focus of the previous chapter was on making a precise determination of the absolute diffuse CXB within the uncertainties imposed by systematics and cosmic variance, and identify its diverse components. This was made possible by the use of a very comprehensive catalog of *Chandra* sources that included those detected at the faintest flux level. While looking for the contributions of the faint discrete sources, it is important to decide as to what threshold one might choose to separate the faint sources from the bright ones. Since this was found to be not easy, we divided the sources into several flux groups and derived the stacked spectra of each flux group, and looked for any trends in the spectral parameters. A similar study was done by Gupta et al. (2009) who divided the sources into two brightness groups. However, this by itself does not help in determining any trends the spectral parameters might have, as well as the one significant threshold below which the contributions of the faintest sources are not at all significant. Since normal galaxies have been predicted to dominate at the current sensitivity limit, it is important to do the grouping based on source type as well and study the spectral characteristics of the various flux groups.

The high signal to noise offered by XMM-*Newton* enabling a high-statistics, accurate determination of the XRB and a precise estimate of its instrumental background allowed us to obtain good constraints on the diffuse CXB parameters. The excellent resolution of the *Chandra* instruments enabled the detection of the faintest X-ray sources, thus allowing for a precise characterization of the extragalactic point

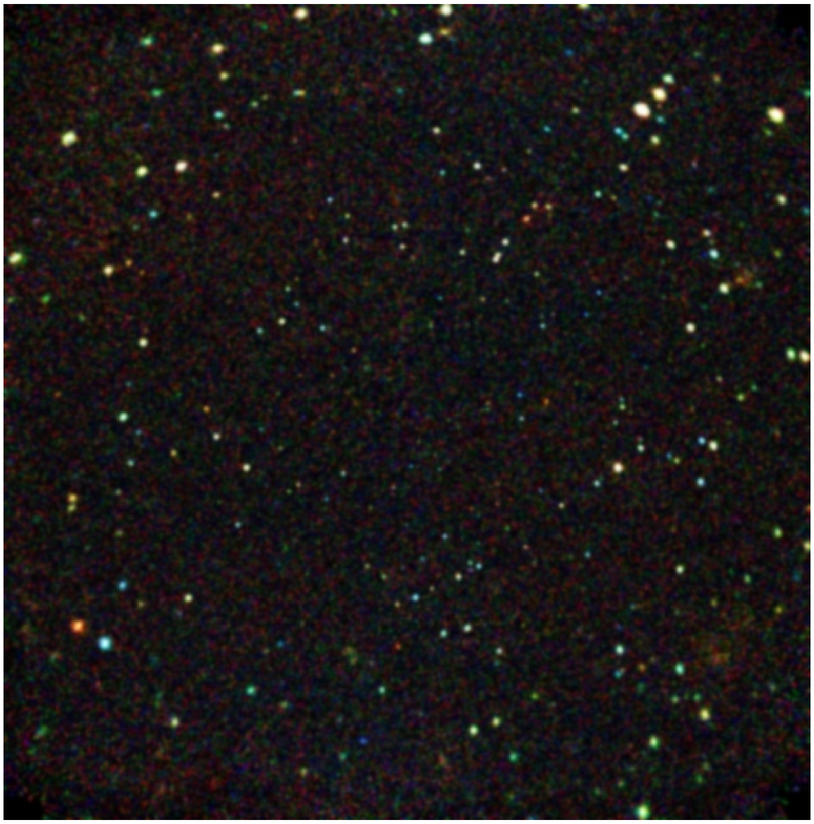

Figure 5.1: *Chandra* Deep Field South ultra-deep 4 Ms survey.

sources. In this chapter, we apply these results to analyze the different types of discrete sources detected by *Chandra*, on the basis of flux and quantify their contributions as we progressively move down the flux scale reaching the current sensitivity limit of $\sim10^{-18}$ ergs cm^{-2} s^{-1}.

5.2 Data selection

Deep sensitive surveys with *Chandra* and XMM-*Newton* have resolved most of the XRB into discrete sources which are mostly AGN (Seyferts and QSO's). At the ROSAT flux limit of 5×10^{-15} ergs cm^{-2} s^{-1}, 70–80% of the XRB is resolved into point sources in the soft band (0.5–2 keV), while *ASCA* and *BeppoSAX* resolved ~23% of the 2–10 keV band and ~30% of the 5–10 keV band respectively. *Chandra*, with its superb sensitivity and positional accuracy, extended identification of discrete sources in the hard band (2–10 keV) resolving ~75% of the XRB. This was followed by the 1 Ms survey (Giacconi et al. 2002) that was extended to 2 Ms (Luo et al. 2008) and finally the 4 Ms (Xue et al. 2011) ultra-deep survey. *Chandra*'s effective area is very energy-dependent and its sensitivity decreases in the hard bands. This study makes use of the point source catalog derived from 4 Ms XMM deep survey in the CDFS by Ranalli et al. 2013. The XMM-CDFS survey aimed at detecting and analyzing obscured AGN which are assumed to make up the bulk of the XRB at higher energies. It has a nominal exposure time of 3.45 Ms which, coupled with the large effective area of XMM-*Newton*, currently gives the best identification of point sources with minimum source confusion as a result of the extensive simulations done, as well as the cross correlation performed with the *Chandra* catalog.

5.3 Spectral extraction

We divided the 740 point sources (Ranalli et al. 2013) into three groups based on the general source type: AGN (568), galaxies (162) and stars (10). The AGN were subsequently divided on the basis of flux $\mathcal{F}$, into six groups as shown in table 5.1. The purpose was to study the dependence, if any, of spectral parameters with flux. This also facilitated spectral extraction with ESAS. Using the region filters and the standard filter expression for pn data, we extracted the selected FOV region from the observation data into a spectral file for each observation by means of the standard ESAS tools.

We derived the cumulative spectra for each of the six flux-selected AGN groups and the four galaxy groups using standard ESAS tools. The average stacked spectrum of the sources from each of the samples was computed using **mathpha**. The corresponding instrumental background was also precisely estimated using the stacked spectrum of the background regions extracted from around each source. The resulting photon files were scaled by the ratio of the source counts and the background counts in the 9–12 keV band. Spectral analysis was done using `XSPEC`[5] (see Arnaud 1996). Since the cut-off radii for the point sources were determined using half energy width

---

[5] XSPEC version: 12.8.2

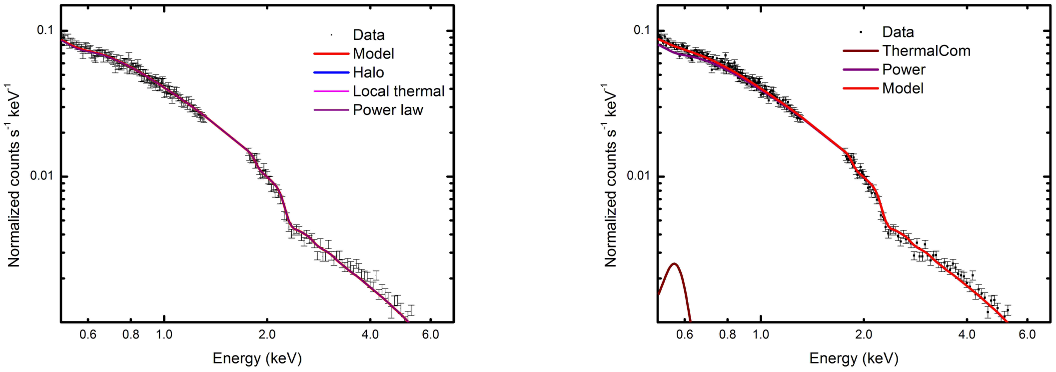

(a)

(b)

Figure 5.2: (a) Stacked spectrum of AGN in the flux group $\mathcal{F} > 10^{-14}$ ergs cm^{-2} s^{-1} fit to an absorbed two-thermal and power law model. (b) The same spectrum fit to a single thermal component and power law.

(HEW), in stead of directly subtracting the total scaled background from the point source spectra we used the same three component model for the point sources also, to model the thermal diffuse components as well as the power law.

5.4 Results

5.4.1 AGN flux groups

In the brightest group ($\mathcal{F} > 10^{-14}$ ergs cm^{-2} s^{-1}) of AGN, there are 7 objects, of which 90–100 % are unobscured sources. Their cumulative spectrum is shown in figure 5.2(a). This is fit to an absorbed power law with a spectral index of 2.08, and two thermal components representing the local and Galactic thermal contributions, thus accounting for some soft excess below 0.7 keV. However, an absorbed power law with a single thermal component gives a much better fit (figure 5.2(b)). The spectrum is characteristic of high luminosity sources ($\mathcal{L}_x > 10^{43}$ ergs s^{-1})—AGN with zero/negligible absorption.

Below this flux level, the AGN spectrum becomes less soft and the spectral index goes down to a value of ~1.6 ($\mathcal{F}$: 10^{-15}–5×10^{-14} ergs cm^{-2} s^{-1}) which is lower than that of the unresolved background (~1.9) before becoming slightly harder towards

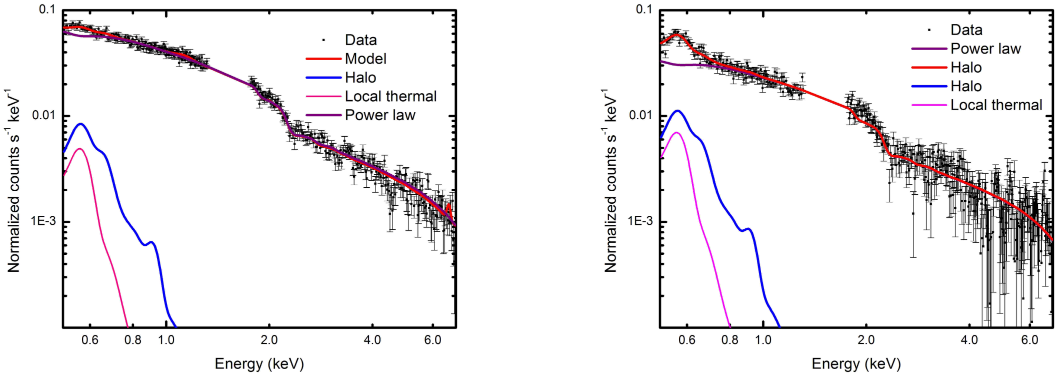

(a) (b)

Figure 5.3: (a) Stacked spectrum of AGN in the flux group $\mathcal{F}$: 10^{-15}–10^{-14} ergs cm^{-2} s^{-1} fit to an absorbed two-thermal and power law model. (b) Stacked spectrum of AGN in the flux group $\mathcal{F}$: $2{\times}10^{-16}$–10^{-15} ergs cm^{-2} s^{-1}.

lower flux groups. The spectrum is (figure 5.3(a)) fit to the same model as the above, and is very similar to the previous one except that the soft excess below 0.6 keV is more obvious. In the next lower group ($\mathcal{F}$: $2{\times}10^{-16}$–10^{-15} ergs cm^{-2} s^{-1}), the spectrum is very similar (figure 5.3(b)) except that the soft excess shows up clearly below ∼0.7 keV. This group contains twenty times more sources than in the second ($\mathcal{F}$: 10^{-15}–5×10^{-14} ergs cm^{-2} s^{-1}) flux group and the integrated effect from all the sources of all redshifts up to $z \simeq 7$ could contribute to the soft excess below ∼0.8 besides the local thermal components. The spectral index becomes much flatter ($\Gamma = 1.58$) at this level signifying that the fraction of absorbed sources is increasing, thus contributing to a harder spectrum. At the same time the unobscured sources still dominate at this flux level.

In the flux group ($\mathcal{F}$: 10^{-16}–2×10^{-16} ergs cm^{-2} s^{-1}) there are 96 sources of which ∼60% are mildly or heavily Compton-thick AGN. The broad band structure reveals absorption edges (figure 5.4(a)) even though the composite nature of the spectrum in terms of redshift, source type and intrinsic column density makes it look more complex. There is no significant increase in spectral index ($\Gamma = 1.58$), only slightly harder, despite an increase in the fraction of obscured sources and a decrease in the number of unobscured sources. However, this group has ∼30% fewer sources than the pre-

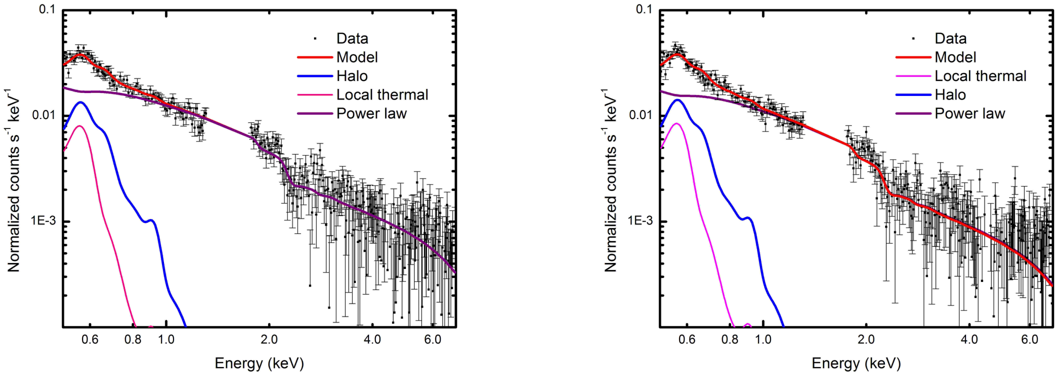

(a)

(b)

Figure 5.4: (a) Stacked spectrum of AGN in the flux group $\mathcal{F}$: 10^{-16}–2×10^{-16} ergs cm^{-2} s^{-1} fit to an absorbed two-thermal and power law model. (b) Stacked spectrum of AGN in the flux group $\mathcal{F}$: 5×10^{-17}–2×10^{-16} ergs cm^{-2} s^{-1}.

vious one. In the next fainter flux group ($\mathcal{F}$: 5×10^{-17}–2×10^{-16} ergs cm^{-2} s^{-1}; see figure 5.4(b)) the spectrum is much softer ($\Gamma = 1.77$) even though the unobscured and obscured fractions are nearly equal and the mildly Compton-thick fraction stays constant. This suggests that obscuration alone cannot explain the variation in the average spectral index and that there is no necessary correlation between flux-based faintness and spectral index. In the faintest flux group ($\mathcal{F}$: 10^{-17}–5×10^{-17} ergs cm^{-2} s^{-1}), the spectrum is clearly harder with a spectral index of $\Gamma = 1.51$ indicating strong absorption (figure 5.5). Unabsorbed fraction contributes only $\sim$5% of all the sources. At this flux level in the CDFS, the power law spectrum is consistent with the XRB spectrum ($\Gamma \approx 1.4$) which requires a significant number of CT sources to fill in the missing fraction at high energies. However, this does not guarantee any tight correlation between intrinsic spectral index and obscuration (Tozzi et al. 2006). The average AGN spectrum shows spectral hardening towards faint flux which is mostly due to obscuration. Unlike the other groups, an additional thermal component with high significance is required for the best fit.

Flux group[a]	Γ[b]	Norm[c]	Temperature[d]	Emission measure[e]
10^{-17}–5×10^{-17}	$1.51^{+0.062}_{-0.06}$	$1.42^{+0.051}_{-0.050}$	$0.192^{+0.014}_{-0.014}$	$0.0014^{+0.0002}_{-0.0002}$
5×10^{-17}–10^{-16}	1.67 ± 0.033	1.69 ± 0.036		
10^{-16}–2×10^{-16}	1.53 ± 0.021	1.94 ± 0.18		
2×10^{-16}–10^{-15}	1.59 ± 0.012	5.27 ± 0.014		
10^{-15}–10^{-14}	1.60 ± 0.0120	5.39 ± 0.02		
10^{-14} and above	2.084 ± 0.0064	5.88 ± 0.021		

[a] Fluxes are in units of erg cm^{-2} s^{-1}

[b] Power law spectral index

[c] Units are photons s^{-1} keV^{-1} cm^{-2} sr^{-1}

[d] In units of keV

[e] In units of cm^{-6} pc. The faintest group needs an extra component with high significance.

Table 5.1: AGN flux group parameters

5.4.2 Galaxy flux groups

Normal galaxies that comprise early-type and late-type star-forming galaxies, constitute a significant fraction of the point sources at the CDFS 4 Ms flux limit. Approximately 22% of the source population used in this study are normal galaxies with a median redshift of ∼0.6 . We divided the whole population into 4 samples based on the same flux ranges that were used for the AGN grouping starting with the faintest flux group. This resulted in a much larger number in the faintest group with 109 sources, the next brighter group getting 31, and the remaining 2 groups 11 galaxies each. To model the spectrum, besides the local thermal contributions, an additional thermal component is also required, since in X-ray bright galaxies X-ray emission is dominated by hot diffuse gas. Table 5.2 shows the spectral parameters. Figures 5.6(a) through 5.7(b) illustrate the spectra with various components for the four flux groups.

5.4.3 Discussion

At the brightest flux level, highly luminous type I AGN form the majority, with only a few mildly obscured sources, and so produce a soft spectrum. Absorbed power law plus local thermal components gives a poor fit while absorbed power law plus

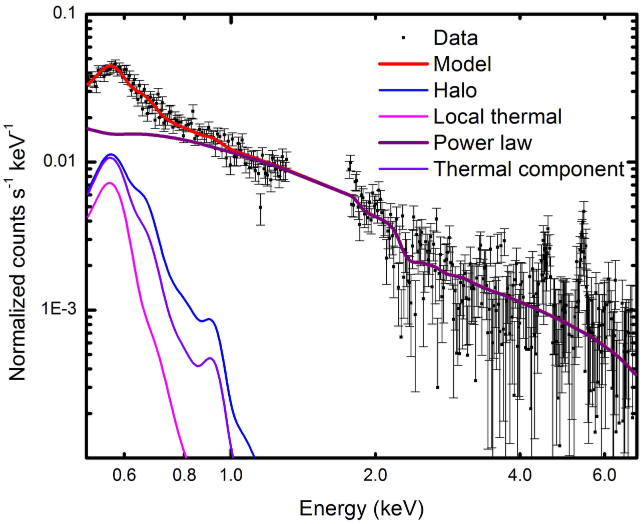

Figure 5.5: Stacked spectrum of AGN in the flux group $\mathcal{F}$: 10^{-17}–5×10^{-17} ergs cm^{-2} s^{-1} fit to an absorbed two-thermal and power law model.

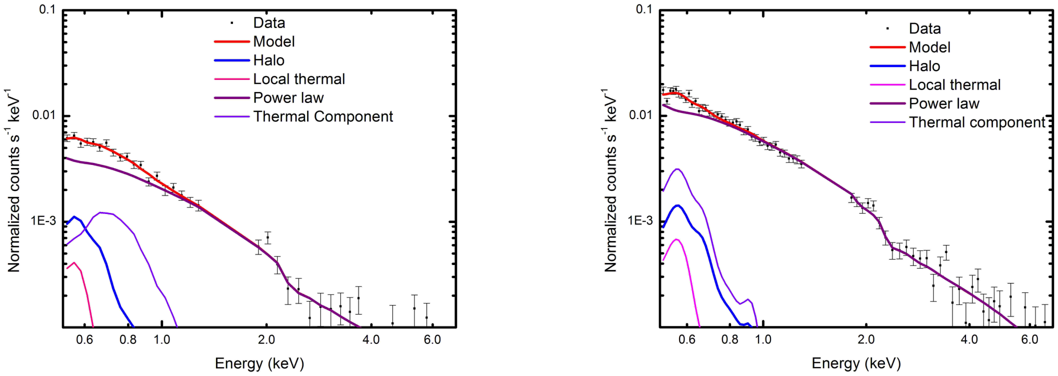

(a)

(b)

Figure 5.6: (a) Stacked spectrum of galaxies in the flux group $\mathcal{F}$: 2×10^{-16}–10^{-15} ergs cm^{-2} s^{-1} fit to an absorbed two-thermal and power law model. (b) Stacked spectrum of galaxies in the flux group $\mathcal{F}$: 10^{-16}–2×10^{-16} ergs cm^{-2} s^{-1}.

Flux group[a]	Γ[b]	Norm[c]	Temperature[d]	Emission measure[e]
10^{-17}–5×10^{-17}	$1.77^{+0.073}_{-0.0735}$	$1.03^{+0.038}_{-0.042}$	$0.18^{+0.065}_{-0.158}$	$0.00027^{+0.00018}_{-0.00019}$
5×10^{-17}–10^{-16}	$1.83^{+0.088}_{-0.089}$	$0.75^{+0.038}_{-0.042}$	$0.21^{+0.030}_{-0.031}$	$0.0011^{+0.00038}_{-0.00037}$
10^{-16}–2×10^{-16}	2.2 ± 0.041	0.30 ± 0.028	0.17 ± 0.033	0.00314 ± 0.001
2×10^{-16}–10^{-15}	$2.088^{+0.157}_{-0.153}$	0.89 ± 0.017	$0.312^{+0.109}_{-0.0385}$	$0.00160^{+0.0009}_{-0.0009}$

[a] Fluxes are in erg cm^{-2} s^{-1}

[b] Power law spectral index

[c] Units are photons s^{-1} keV^{-1} cm^{-2} sr^{-1}

[d] In units of keV

[e] In units of cm^{-6} pc

Table 5.2: Galaxy flux group parameters

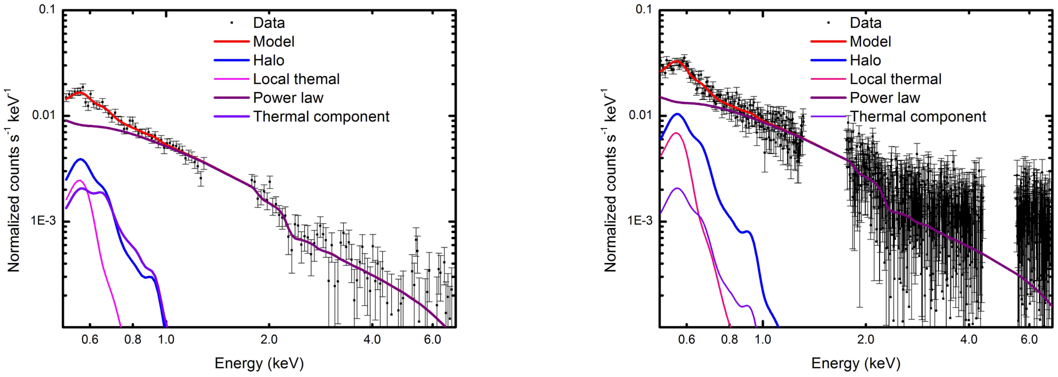

(a) (b)

Figure 5.7: (a) Stacked spectrum of galaxies in the flux group $\mathcal{F}$: 10^{-17}–5×10^{-17} ergs cm^{-2} s^{-1} fit to an absorbed two-thermal and power law model. (b) Stacked spectrum of galaxies in the flux group $\mathcal{F}$: 5×10^{-17}–10^{-16} ergs cm^{-2} s^{-1}.

a single component gives a good fit. It appears that the area of spectral extraction is too small for the local components to be significant. For the lower flux groups, the spectra have a highly complex structure due to an admixture of several source types with varying luminosities and redshifts and get modified by a combination of obscuration, reflection, line emission features. In the averaged spectra, some of these features are smoothed out and some others are enhanced.

While the above limitations make it very difficult to derive definitive conclusions regarding the mechanisms that are presumed to power the AGN based on the unification scheme, we can still deduce some general spectral properties from our analysis.

Even though the average AGN spectrum hardens toward very faint fluxes, the majority of the sources being absorbed ones at these flux levels, we do not see a tight correlation between spectral index and flux, and the spectrum can be characterized by an average $\Gamma \approx 1.6$ if the brightest group is excluded (figure 5.8). Such a hard spectrum is consistent with the flat XRB spectrum and provides the hard sources necessary to fill in the missing fraction of the XRB at higher energies thereby providing a possible solution to the spectral paradox (Mushotzky et al. 2000). Except for the brightest and the faintest groups, the spectrum is reasonably well described by an absorbed power law, and local thermal contributions whose parameters were frozen to the best fit values obtained from the DXB analysis. At the brightest flux level, the above model is not significantly better than an absorbed power law model, while an absorbed power law model plus a single thermal component gives a better fit. For the faintest group, where the source density is ~50% larger, and the area of spectral extraction is ~50% smaller, an additional thermal component with high significance, is necessary to obtain a good fit. This indicates the spectral complexity of the AGN and the need to explore more meaningful modeling that is capable of shedding light on the elusive nature of AGN X-ray emission which involves subtle components in

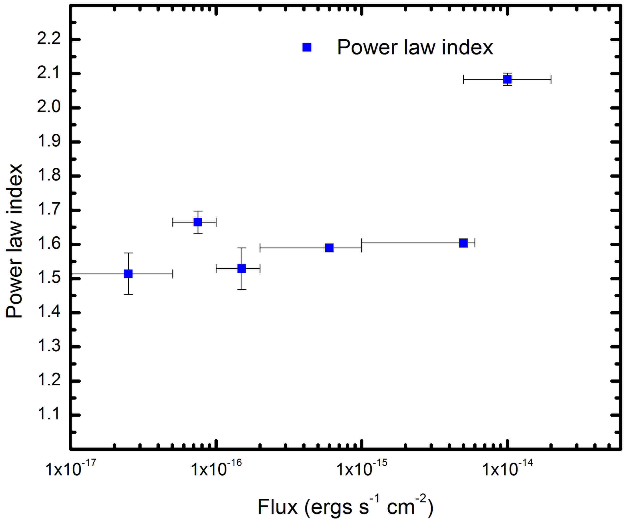

Figure 5.8: Variation of AGN spectral index with flux. Flux units are erg cm^{-2} s^{-1}.

addition to the continuum source driving the central engine.

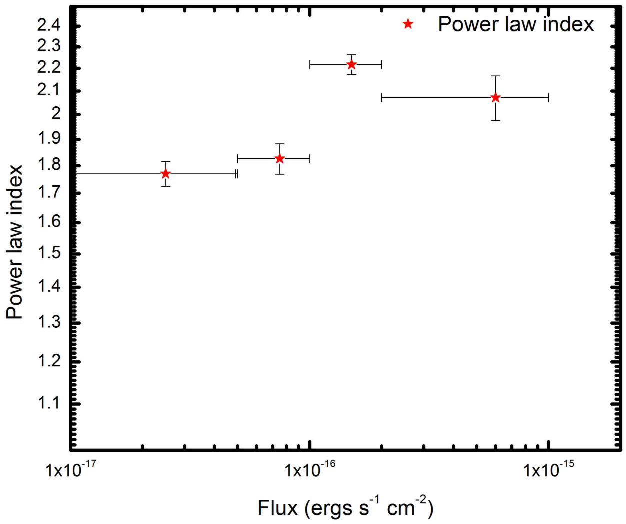

Figure 5.9: Variation of galaxy spectral index with flux. Flux units are erg cm^{-2} s^{-1}.

The galaxy spectrum is softer when compared to that of AGN in each flux group implying that absorbed sources probably do not make a significant contribution to galaxy number counts. Over the whole flux range the spectral index shows more dispersion than it does in the case of AGN. At the faintest flux level, the spectra become harder which may be indicating the presence of late-type star forming galaxies that, together with fainter early-type galaxies, have been predicted to outnumber the AGN population in the faintest flux regime. This underscores the need for ultra-deep surveys capable of probing fainter depths to uncover hidden X-ray populations.

Chapter 6

Summary

The diffuse cosmic X-ray background (CXB) has creatively engaged astrophysicists ever since its discovery in 1962. In the ensuing decades, tremendous progress was made in the analysis and understanding of its diverse origins and mechanism. Pencil beam surveys using focusing telescopes with ever-increasing sensitivity have resolved most of the XRB into faint discrete sources. At the same time there still remains discovery space in the faint flux regime which is beyond the capabilities of the most advanced telescopes.

Above $\sim$1.2 keV the CXB is almost exclusively attributed to faint discrete sources while below 1.2 keV its spectral and spatial structure is very complex. Besides the dominant contribution from point sources, the diffuse X-ray background is made up of at least four components—a thin thermal component in CIE at a temperature of $\sim$1 million kelvin, a hotter component in CIE at $\sim$2 million kelvin called the Galactic halo, solar wind charge exchange (SWCX) and the emission from the putative warm hot intergalactic medium (WHIM). Since all these components are composed of hundreds of emission lines that are indistinguishable from each other, disentangling the various components presents a very challenging task. Besides, weak diffuse emission due to exotic phenomena such as dark matter decay could also contribute below the current sensitivity limit.

A practicable approach to this problem in order to make reliable inferences on the contributions of DXB components is to apply good models to valid data with high statistics. With this in mind, for this work, we selected high quality data, from the well-surveyed sky direction—the *Chandra* Deep Field South (CDF-S)—with 4 Ms of observing time. The CDFS is arguably the most intensively studied direction with panchromatic coverage, and thus provides a most comprehensive catalog of sources with minimum source confusion and Edington bias, enabling us to make a precise determination of the absolute CXB.

For our investigation of the cosmic soft X-ray background we made use of 33 XMM-*Newton* observations of the *Chandra* Deep Field South (CDFS) with a nominal exposure time of 3.45 Ms to study the diffuse X-ray background in the energy range 0.5–8 keV. Here we used to good advantage the large effective area of the XMM-*Newton* telescope coupled with its reasonably good angular and spectral resolution and the *Chandra*-detected catalog of 740 point sources along with the XMM and extended sources to make an accurate determination of the spectral properties of the CXB, and to derive its parameters and calculate intensities in several bands in the range 0.5–8 keV.

We used the standard SAS and ESAS routines to derive clean X-ray maps filtered of all non-X-ray events. To analyze the DXB background, we made region masks in the form of region list files in fits format, in both detector and sky coordinates. Additional region selection from the full FOV was done by including the appropriate region file in the filter expression. We limited our analysis to the *Chandra* exposure region to include all the *Chandra*-detected sources. A polygonal region in the XMM event map, that encloses the *Chandra* FOV, is chosen whose perimeter corresponds to $\sim$30 percent of the maximum exposure thus excluding the region outside the polygon where the large off-axis angles introduce greater uncertainty in determining the PSF.

To make a precise estimation of the instrumental background we used the standard ESAS routine `pnback` which creates not only a model quiescent particle background spectrum for user-defined regions of the detector, but also produces background subtracted and exposure-corrected images. The instrumental background is subtracted from the total spectrum during XSPEC fitting.

Spectral extraction was done using ESAS routines. The total spectrum includes the truly diffuse X-ray background, the instrumental background and the flux remaining outside the HEW of the *Chandra* sources. The selected FOV region from the observation data was extracted into a spectral file for each observation using the region filters and the standard filter expression for pn data.

The thirty two spectra belong to observations from time periods spread over several years. Hence the response can change from observation to observation. Also one has to deal with systematics introduced by varying components. In our case, contamination from SWCX was a significant factor. Taking all these into account, we fit the thirty two data sets simultaneously thus obtaining tighter constraints than we would if we did a simple fit to the merged spectra. This method also allowed us to analyze the temporally varying component of X-ray emission due to solar wind charge exchange (SWCX) .

We were able to obtain a robust fit linking all the parameters. We also performed the fit by adding up all the thirty two spectra using **mathpha**, which gives an average over the thirty two data sets; the results from both fits are in good agreement. The extragalactic parameters for the CDFS are consistent with those of HM06 within the 2σ limits.

To begin with, we used a simple three-component model consisting of a two thermal components in CIE to model the Galactic components and an absorbed power law for the extragalactic emission. The results showed good agreement with previous work within errors. Having verified the quality of our data and the robustness of our procedure, we employed more complex models to study the temporally varying component of SWCX. Since, in the simple model, we have no way of measuring SWCX, the residual flux is shared between the two thermal components. We used the independently determined values of the local bubble parameters and fixed them before applying the more complex models to our data.

To estimate SWCX, we used gaussian models in which the prominent ions responsible for SWCX emission were included as δ functions. Ideally all the SWCX ions should be included to accurately model SWCX. However, owing to the incomplete nature of the atomic data on charge exchanging plasma as well as the limited resolution of the CCD detectors, we could only model a few dominant lines. Considering that O VII and O VIII constitute the dominant SWCX lines, this is not a serious constraint, and the results justify the model we have used. The linear best fit of the O VII vs O VIII line intensities gives a slope is 0.343. We noticed a significant excess at the

Ne ɪx energy of 0.92 keV and added another δ function which slightly improved the fit. This implies a higher-than-solar abundance for Ne ɪx which is also an important diagnostic of astrophysical plasma.

A sophisticated model, known as the ACX model due to Smith et al. (2014), was also used to model SWCX. It was found that the ACX model while giving abundance-based weight to all SWCX ions gives a re-scaled measure of the oxygen line intensities and attributes the excess flux to the halo. This is to be expected given the fact that the model does not consider actual cross sections and relies on rough estimates of ion densities, both of which are critical when the temporal variations of SWCX are to be modeled. The ACX norms only give a scaled emissivity of CX plasma. The model is an approximation that does not include the actual cross section of the charge exchange process itself, and so the norm has no physical use except as a relative scaling (see Smith et al. 2014). At the same time, the model can be used as an excellent diagnostic tool to predict SWCX and to confirm the results from other models. Since the model can treat SWCX for only one temperature at a time rather than multiple temperatures, it has limitations when dealing with such wide swings in thermal conditions as exist in stellar coronae. The ACX model can potentially be a powerful tool for characterizing SWCX if a multi-temperature treatment of the CX-ing plasma is accomplished along with the inclusion of an accurate treatment of CX cross sections. Fortunately for our purpose, such a sophisticated analysis of the SWCX was not required owing to the low degree of contamination. The simpler models—the gaussian models that we used—adequately explain and quantify the extent of CX contamination in our data reasonably well and serve to constrain the SXRB parameters to a high degree of accuracy.

Our data had been chosen from a nine-year period that spanned a solar cycle starting with the solar maximum, with the secondary goal of studying the temporal variation of SWCX. During solar maximum, up to three CME's can occur per day, which can be accompanied by solar flares, resulting in a sudden rise in solar wind flux which is reflected in a corresponding enhancement in the heliospheric SWCX emission. Extreme solar phenomena are characterized by temperatures of tens of millions of kelvin leading to the release of high charge state ions at heightened levels. The important solar wind ions producing SWCX emission are O VII and O VIII. During solar maximum, the relative abundances of these ions can jump to higher levels leading to higher charge transfer reactions resulting in spurts of heliospheric X-ray intensities. We derived the O VII and O VIII intensities for all the thirty two observations and studied the various correlations. Oxygen line intensities are found to be tightly correlated. They are also correlated with the ACX norms. We also compared these time-varying norms against the solar proton flux which again revealed mutual correlation. Thus our method provided us with an effective means of studying heliospheric SWCX using several models, and all the models gave consistent results within systematic and statistical errors.

We obtained marginally higher intensities than those of HM06 for the extragalactic component in the 1–2 keV and 2–8 keV which could indicate some truly diffuse flux and/or unresolved faint sources. We got a total power law normalization of 11.38 ± 0.011 photons cm^{-2} s^{-1} sr^{-1} at 1 keV which is very close to the value obtained by De Luca and Molendi (2004).

Having obtained very good constraints on the DXB parameters, we proceeded to derive the spectra of the *Chandra* sources. To examine any trends in the spectral parameters with decreasing flux we divided the point sources into flux groups. This is relevant to the study of the DXB in view of the fact that a precise characterization of the DXB entails a determination of the faint flux limit at which the unresolvable flux becomes insignificant. We derived the average spectra of the various flux groups, analyzed the various components and obtained some interesting results. While an average spectral index of 1.6 adequately characterizes the AGN, a higher value of 1.95 describes the galaxies. Obscuration seems to effect some hardening of the average spectrum towards fainter fluxes.

The average spectrum very bright AGN ($\mathcal{F} > 10^{-14}$ ergs cm^{-2} s^{-1}) can be fit to a power law. However, AGN spectrum is more complex than the simple picture described by the power law. An additional thermal/black body component improves the fit. Obscured AGN spectra have many subtle features. At the faintest flux level, an additional thermal component over and above the two local thermal components are needed to model the spectrum. The average galaxy spectrum is softer when compared to that of the AGN. For all the flux groups, an additional thermal component is required to get a good fit, as expected. The emission measures show a clear trend in the case of all but the brightest flux group which has a much higher temperature, probably indicating the presence of starburst galaxies.

Bibliography

[1] [Anders & Grevesse 1989] Anders, E., & Grevesse, N. 1989, Geochim. Cosmochim. Acta, 53, 197

[2] [Arnaud & Dormer 2002] Arnaud, K., & Dormer, B. 2002, XSPEC: An X-Ray Spectral Fitting Package, User's Guide for Version 11.2.x (Greenbelt, MD:GSFC)

[3] [Baldi et al. 2002] Baldi, A., & Molendi, S., et al. 2002, ApJ, 564, 190

[4] [Bates & Dalgarno 1962] Bates, D. R., & Dalgarno, 1962, "Atomic and Molecular Processes," Academic Press, New York

[5] [Bennet et al. 2003] Bennet, C. L., et al. 2003, ApJS, 148, 1

[6] [Bloch et al. 1986] Bloch, J. J., Jahoda, K., Juda, M., McCammon, D., Sanders, W. T., & Snowden, S. L. 1986, ApJ *Lett*, 308, L59

[7] [Borgani et al. 2004] Borgani, S., et al. 2004, MNRAS, 348, 1078

[8] [Bowyer et al. 1968] Bowyer, C. S., et al. 1968, Nature, 217, 32–34

[9] [Brandt et al. 2001] Brandt, W. N., et al. 2001, AJ, 122, 1

[10] [Burrows et al. 1985] Burrows, D. N., Nousek, J. A., Traux, R. J., Garmire, G. P., & Singh, K. P. 1985, Bull. Am. Astron. Soc. 17:883

[11] [Burrows & Mendenhall 1991] Burrows, D. N., & Mendenhall, J. A. 1991, Nature, 351, 629

[12] [Cen & Ostricker 1999] Cen, R., & Ostricker, J. P. 1999, ApJ, 514, 1

[13] [Cox & Anderson 1982] Cox, D. P., & Anderson, P. A. 1982, ApJ, 253, 268

[14] [Cox 1998] Cox, D. P. 1998, Lecture Notes in Physics 506, The Local Bubble and Beyond, ed. D. Breitschwerdt, M. J. Freyberg, & J. Trümper (Berlin: Springer Verlag), 121

[15] [Cravens et al. 2000] Cravens, T. E., et al. 2000, ApJ, 532L, 153C

[16] [Croft et al. 2001] Croft, R. A. C., et al. 2001, ApJ, 557, 67

[17] [Dalgarno et al. 1966] Dalgarno, A., et al. 1966, MNRAS, 131, 311D

[18] [Ehle et al. 2008] Ehle, M. et al. 2008, XMM-*Newton* User's Handbook, European Space Agency

[19] [Fabian et al. 1992] Fabian, A. C., & Barcons, X. 1992, ARA&A, 30, 429

[20] [Field & Henry 1964] Field, George B., & Richard C. Henry, 1964, ApJ, 140, 1002

[21] [Frisch & York 1983] Frisch, P. C., & York, D. G. 1983, ApJ, 271, 59

[22] [Fukugita et al. 1998] Fukugita, M., Hogan, C. J., & Peebles, P. J. E. 1998, ApJ, 503, 518

[23] [Galeazzi et al. 2007] Galeazzi, M., Gupta, A., Covey, K., & Ursino, E., et al. 2007, ApJ, 658, 1081

[24] [Galeazzi et al. 2014] Galeazzi, M., et al. 2014, Nature, 512, 171

[25] [Garmire et al. 1992] Garmire, et al.

[26] [Gendreau et al. 1995] Gendreau, K. C., et al. 1995, PASJ, 47, L5

[27] [Georgantopoulos et al. 1996] Georgantopoulos, I., et al. 1996, MNRAS, 280, 276

[28] [Giacconi et al. 1962] Giacconi, R., & Rossi, B. B. 1962, Phys. Rev. Lett., 9, 439

[29] [Giacconi et al. 2002] Giacconi, R., et al. 2002, ApJS, 139, 369

[30] [Gilli et al. 2007] Gilli, R., et al. 2007, A&A, 463, 79

[31] [Gupta et al. 2009] Gupta, A., et al. 2009, ApJ, 702, 270–276

[32] [Hasinger et al. 1998] Hasinger, G., et al. 1998, A&A, 329, 482

[33] [Henley & Shelton 2007] Henley, D. B., & Shelton, R. L. 2007, ApJ, 661, 304

[34] [Henley & Shelton 2010] Henley, D. B., & Shelton, R. L. 2010, ApJ, 187, 388

[35] [Henry et al. 1968] Henry, R. C., et al. 1968, ApJ, 153L, 11

[36] [Hickox & Markevitch 2006] Hickox, R. C., & Markevitch, Maxim, 2006, ApJ, 645, 95

[37] [Ishisaki et al. 2007] Ishisaki, Y., et al. 2007, PASJ, 59S, 113I

[38] [Juda 1988, PhD thesis] Juda, M. 1988, PhD thesis, University of Wisconsin, Madison

[39] [Kaastra et al. 2008] Kaastra, K. S., Paerels, F. B. S., Durret, F., & Schindler, S., & Richter, P. 2008, SSRv, 134, 155K

[40] [Kellermann et al. 2008] Kellermann, K. I., et al., 2008, ApJS, 179, 71

[41] [Koyama et al. 2007] Koyama, K., et al. 2007, PASJ, 59, S23

[42] [Kuntz & Snowden 2000] Kuntz, K. D., & Snowden, S. L. 2000, ApJ, 543, 195

[43] [Kuntz et al. 2001] Kuntz, K. D., et al. 2001, ApJ, 548, L119

[44] [Landy & Szalay 1993] Landy, S. D., & Szalay, A. S. 1993, ApJ, 412, 64L

[45] [Lehmer et al. 2012] Lehmer, B. D., et al. 2012, ApJ, 752, 46

[46] [Liu et al. 2016] Liu, W., et al. 2016, ApJ, submitted

[47] [Longair 1992] Longair, M. S. 1992, ”High Energy Astrophysics”, Cambridge University Press, Cambridge

[48] [Luo et al. 2010] Luo et al. 2010, ApJS, 187, 560

[49] [McCammon et al. 1983] McCammon, D., Burrows, D. N., Sanders, W. T., & Kraushaar, W. L. 1983, ApJ, 269, 107

[50] [McCammon & Sanders 1990] McCammon, D., & Sanders, W. T. 1990, ARA&A, 28

[51] [MacCammon et al. 2002] McCammon, D., et al. 2002, ApJ, 576, 188

[52] [Madau et al. 1994] Madau, P., et al. 1994, MNRAS, 270, L17

[53] [Marshall & Clark 1980] Marshall, F. J., & Clark, G. W. 1980, BAAS, 14R, 975M

[54] [Mendenhall & Burrows 2001] Mendenhall, J. A., & Burrows, D. N. 2001, ApJ, 563, 716

[55] [Mushotzky et al. 2000] Mushotzky, R. F., Cowie, L. L., Barger, A. J., & Arnaud, K. A., et al. 2000, Nature, 404, 459

[56] [Nicastro et al. 2005] Nicastro, F., et al. 2005, Nature, 433, 495

[57] [Peebles 1980] Peebles P. J. E. 1980, ”The Large Scale Stucture of the Universe”, Princeton Univ. Press, Princeton

[58] [Ranalli et al. 2013] Ranalli, P., et al. 2013, A&A, 555, A42

[59] [Rauch et al. 1998] Rauch, M., et al. 1998, ASSL, 231, 291R

[60] [Read & Ponman 2003] Read, A. M., & Ponman, T. J. 2003, A&A, 409, 395

[61] [Robertson et al. 2003] Robertson, I. P., Cravens, T. E., & Snowden, S. L., American Geophysical Union, 2003, SH11C1126 (2003)

[62] [Romer et al. 2001] Romer, A. K. Viana, P. T. P., Liddle, A. R., & Mann, R. G. 2001 ApJ, 547, 504

[63] [Rosati et al. 2002] Rosati, P., et al. 2002, ApJ, 566, 667

[64] [Sanders et al. 1977] Sanders, W. T., Kraushaar, W. L., Nousek, J. A., & Fried P. M., et al. 1977, ApJ, 217L, 875

[65] [Sanders et al. 2000] Sanders, W. T., Edgar, Richard J., Kraushaar, W. L. McCammon, D., Morgenthaler, J. P., et al. 2001, ApJ, 554, 594

[66] [Shull & Slavin 1994] Shull, J. M., & Slavin, J. D. 1994, ApJ, 427, 784

[67] [Smith et al. 2001] Smith, R. K., Brickhouse, N. S., Liedhal, D. A., & Raymond, J. C. 2001, ApJ, 556, L91

[68] [Smith et al. 2014a] Smith, R. K., et al. 2014, ApJ, 787, 77

[69] [Smith et al. 2014b] Smith, R. K., & Foster A., 2014, The AtomDB Charge Exchange Model, an ACX manual

[70] [Smith & Cox 2001] Smith, R. K., & Cox, D. P. 2001, ApJS, 134, 283

[71] [Smith et al. 2007] Smith, R. K., et al. 2007, PASJ, 59, S141

[72] [Snowden et al. 1991] Snowden, S. L., Mebold, U., Hirth, W., Herbstmeier, U., & Schmitt, J. H. M., et al. 1991, Science, 252, 1529S

[73] [Snowden et al. 1994a] Snowden, S. L., McCammon, D., Burrows, D. N., & Mendenhall, J. A. 1994, ApJ, 424, 714

[74] [Snowden et al. 1998] Snowden, S. L., Egger, R., Finkbeiner, D. P., Freyberg, M. J., & Plucinsky, P. P. 1998, ApJ, 493, 715

[75] [Soltan et al. 1996] Soltan, A. M., et al. 1999, A&A, 349, 354

[76] [Spitzer & Greenstein 1951] Spitzer, L. J., & Greenstein, J. L. 1951, ApJ, 114, 407S

[77] [Tripp & Sandage 2002] Tripp, T. M., & Sandage, B. D. 2000, ApJ. 542, 42

[78] [Ursino & Galeazzi 2006] Ursino, E., & Galeazzi M., 2006, ApJ, 652, 1085

[79] [Weinberg et al. 1997] Weinberg, D. H., Miralda-Escude, J., Hernquist, L., & Katz, N. 1997, ApJ, 490, 564

[80] [Wright et al. 1994] Wright et al. 1994, ApJ, 420, 450–456

[81] [Xue et al. 2011] Xue et al. 2011, ApJ, 195, 1–31